FIELD OBSERVATIONS AND NUMERICAL MODELS OF A PLEISTOCENE-HOLOCENE FEEDER DYKE SWARM ASSOCIATED WITH A FISSURE COMPLEX TO THE EAST OF THE TATARA-SAN PEDRO-PELLADO COMPLEX, SOUTHERN VOLCANIC ZONE, CHILE

Javiera Ruz [a,b], John Browning [a,b,c], José Cembrano [a,b*], Pablo Iturrieta[d]

Muriel Gerbault [e], Gerd Sielfeld [f]

a. Department of Structural and Geotechnical Engineering, Pontificia Universidad Católica de Chile, Santiago, Chile.
b. Andean Geothermal Centre of Excellence (CEGA), Universidad de Chile, Santiago, Chile.
c. Department of Mining Engineering, Pontificia Universidad Católica de Chile, Santiago, Chile.
d. Helmholtz Centre Potsdam, GFZ German Research Centre for Geosciences, Potsdam, Germany.
e. GET/UMR5563 (UPS, CNRS, IRD, CNES); Obs. Midi-Pyrénées, Université P. Sabatier, Toulouse, France
f. Prisma Austral Foundation, Punta Arenas, Chile.

*Corresponding author e-mail: jbrowning@ing.puc.cl

ABSTRACT

In active volcanic chains, the crustal redistribution and storage of hydrothermal and/or magmatic fluids can result in the development of ore deposits, geothermal reservoirs and surficial hydrothermal and volcanic expressions. Magma is transported through the lithosphere as dykes which, during periods of unrest, may feed eruptions at the surface. The propagation path of dykes is influenced by the crustal stress field and can be disturbed and whether a dyke reaches the surface to feed an eruption is influenced by the crustal stress field. The propagation path of dykes can be disturbed by crustal heterogeneities such as contrasting rock units or faults. Moreover, as dykes propagate, they themselves influence the surrounding stress field through processes of stress transfer, crustal deformation and seismic failure. The result is the formation of arrested dykes, as well as contrasting strike and dip angles and dyke segmentation. Here, we study the mechanisms of dyke injection and the role played in modifying the stress field and potential propagation paths of later dyke injections. To do this we combine field data from an eroded and well-exposed shallow feeder dyke swarm with a suite of two-dimensional FEM numerical models. We mapped 35 dyke segments over a ~1 km long dyke swarm exposed ~5 km to the East of Pellado Volcano, in the Tatara-San Pedro-Pellado (TSPP) volcanic complex, Southern Volcanic Zone of the Andes. Detailed mapping of the swarm elucidates two preferential strike orientations, one ~N80ºE and the other ~N60ºE. Our numerical models simulate both the TSPP volcanic complex and the studied dyke swarm as zones of either magmatic excess pressure or as a rigid inclusion. The crustal segment hosting the volcanic complex and dykes is modelled using an elastic domain subjected to regional compression in select model cases. Model outputs provide the stress and strain fields resulting from the different geometries and applied boundary loads. The model results indicate that individual dyke injections can locally rotate the principal stresses such as to influence the range of orientations over which later dykes will form. The orientation of the maximum principal stress (σ_1) at the dyke tip ranges over 60º (±30º either side of the dyke tip) indicating that the strike orientation of later dykes will fall within this range. The effect of adding a bulk regional compression is to locally increase the magnitude of favorably oriented tensile stresses in the bedrock but to reduce the range of σ_1 orientations to 40º (±20º). This implies that under a far-field transpressive

stress regime, as is common in Andean settings, regional dyke swarms will tend to maintain their strike orientation parallel to the regional bulk stress. These results should be accounted for when studying periods of volcanic unrest in order to discern the location and orientation of potential fissure eruptions in active volcanic areas such as the Southern Volcanic Zone of the Andes.

Keywords: Dyke propagation paths; Southern Volcanic Zone; Numerical modelling; Fissure eruptions; Arc volcanism; Transpressional convergence.

1. INTRODUCTION

In active volcanic chains, the crustal redistribution and storage of hydrothermal and/or magmatic fluids can result in the development of ore deposits, geothermal reservoirs and surficial hydrothermal and volcanic expressions. Particularly, dykes are thought to be the most efficient mechanism of magma transport through the upper brittle crust. Dykes that reach the surface feed both elongated fissure eruptions and discrete volcanic vents (Acocella and Neri, 2009). The development of dyke swarms is commonly related to the orientation of principal stresses such that dykes propagate along the plane containing the maximum and intermediate principal stress axis (e.g. Anderson, 1951; Nakamura, 1977). The result is aligned volcanic features such as elongated regional dyke swarms and preferential alignment of volcanic centres and fissures at the surface (Rooney et al., 2011; Sielfeld et al., 2017). However, crustal discontinuities and heterogeneities, such as brittle faults, bedding structures, and elastic (soft or rigid) inclusions, also influence dyke transport and emplacement in the crust (e.g. Nakamura, 1977; Shaw, 1980; Delaney et al., 1986; Gudmundsson and Andrew, 2007; Andrew and Gudmundsson, 2008). For example, a propagating dyke may take advantage of optimally oriented pre-existing joints or fractures to continue its path, in which case the end-member dyke orientation may not necessarily record the accurate state of crustal stress at the time of injection (Shaw, 1980; Delaney et al., 1986; Emerman and Marrett, 1990; Tibaldi et al., 2008; Cembrano and Lara, 2009; Spacapan et al., 2016).

Moreover, propagating dykes are dynamic features which likely influence and iteratively modify the local crustal stress field around them. This has been shown through interpretations of induced stress transfer and deformation, triggering of seismic failure and structural geology field work and stress inversion (e.g. Hill, 1977; Chouet et al., 1996; Roman and Cashman, 2006; Tibaldi & Bonali, 2017). For example, during the 2014-2015 Bárðarbunga-Holuhraun rifting event in Iceland, a substantial amount of seismicity (>30,000 volcano-tectonic events (VTs)) was detected (Sigmundsson et al., 2015; Gudmundsson et al., 2014; Woods et al., 2018; Ágústsdóttir et al., 2019). The seismicity was associated with the growth of a segmented dyke over a length of around 48 km and eventually produced an effusive fissure eruption at the Holuhraun lava field (Ágústsdóttir et al., 2016). In this case, seismicity was primarily related to stress transfer and the rupture

of critically stressed faults around the propagating dyke (Gudmundsson et al., 2014; Woods et al., 2018; Ágústsdóttir et al., 2019). It is hence essential to understand how the emplacement and propagation of dykes alters the crustal stress field and to understand how these processes influence the emplacement of later magmatic intrusions.

Dykes form perpendicular to the least compressive stress and hence extensional tectonics have commonly been considered as a requirement for the formation of vertical dykes and associated volcanism (e.g. Acocella and Funiciello, 2010). Thus, regional stresses at convergent margins are apparently not favourable for the formation of vertical dykes, and instead should promote dyke arrest and sill formation (e.g. Dahm., 2000a; Kavanagh et al., 2006; Menand et al., 2010). However, rotation of the principal stresses may permit local transtension in an intra-arc region which can be accommodated by deformation partitioning (e.g. Pérez-Flores et al., 2016; Sielfeld et al., 2019b), crustal heterogeneities (e.g. Drymoni et al., 2020), load of a volcanic edifice (e.g. Dahm., 2000a; Gudmundsson, 2002; Maccaferri et al., 2011), and the loading effect of crustal reservoirs (e.g. Gudmundsson, 2006). Moreover, others have shown that in purely compressional settings magma can also migrate and reach the surface through systems of thrust and normal faults, and folds (e.g. Kalakay et al., 2001; Galland et al., 2003; Galland et al., 2007; Tibaldi, 2008; Galland et al., 2016). Therefore, understanding the mechanics of dyke emplacement in transpressive settings remains a fundamental problem through which insights on the interplay between magma transport, crustal deformation and tectonic setting can be gained.

In this study, we investigate a feeder dyke swarm in the Tatara-San Pedro-Pellado volcanic (TSPP) complex (36ºS) in the Southern Volcanic Zone of the Andes, where a strong spatial relation exists between NE-striking oblique and dip-slip faults and NE-ENE striking Pleistocene-Holocene dykes (Figure 1). The aim of this work is to understand the stress field that operated during the emplacement of a series of different dyke segments. We propose that such study is necessary in order to understand the dynamic evolution of dyke swarms during emplacement in transpressive crustal regimes. The results are likely to be important for forecasting the location and timing of future fissure eruptions.

2. VOLCANO TECTONICS OF THE SOUTHERN ANDES

The Chilean Andean margin is currently characterized by dextral oblique convergence, (ca. N78ºE at a rate of ca. 6.6 cm/year) between the Nazca and South American plates, that has been consistently maintained during the last 20 Ma (Pardo-Casas & Molnar, 1987) (Figure 1). Subduction related processes in the Chilean Andean margin have been ongoing since at least the Early Jurassic (~200 Ma) (Stern, 2004) when the volcanic arc was in the position of the present-day Coastal Cordillera. Combinations of several plate-margin-scale processes, throughout this time, resulted in an overall eastward migration of the volcanic arc to its present location (e.g. Stern, 2004).

The Southern Volcanic Zone (SVZ) makes up the volcanic arc of the Andes between 33ºS and 46ºS and is divided into four segments (Stern, 2004). These segments form in close spatial relation to latitudinal differences in basement characteristics such as crustal thickness (Tassara & Yáñez, 2003; Stern, 2004), and petrographical, geochemical and isotopic variations of erupted products (Hildreth and Moorbath, 1988; López-Escobar et al., 1995; Dungan et al., 2001; Cembrano and Lara, 2009). The southernmost segments (37ºS – 46ºS) are constructed over Cenozoic plutonic and metamorphic rocks (e.g. Charrier et al., 2002). Intra arc tectonics in the southernmost segments is dominantly governed by the margin parallel Liquiñe Ofqui Fault System (Figure 1). The northernmost segments' (33ºS – 37ºS) of the SVZ are characterized by a thick Meso – Cenozoic volcano sedimentary cover (e.g. Tapia et al., 2015; Cembrano and Lara, 2009 and references therein) and overlie margin-parallel Cenozoic folds and thrust faults that represent the westernmost expression of the Aconcagua and Malargüe fold and trust belts (e.g. Giambiagi and Ramos, 2002).

Active tectonic features in the transitional segment of the SVZ (34.5º-37ºS) are either poorly developed margin-parallel strike-slip faults or well-defined Andean Transverse Faults (e.g. Piquer et al., 2018; Sielfeld et al., 2019b). Current NE-trending shortening at ~36ºS is suggested by the focal mechanism of the Mw 6.2 crustal earthquake on the ~N10ºE Melado fault (Cardona et al., 2018) (Figure 2). The geometry and nature of this crustal fault is constrained by > 600 aftershocks and by a dextral strike-slip moment tensor (from NEIC and GCMT catalogues). Cardona et al. (2018) also registered crustal events

along the WNW- and NE-striking Laguna Fea and Troncoso faults respectively, in the SW corner of the Laguna del Maule (Figure 2). Active seismicity to the north of the study area (~35.5ºS) also shows margin parallel and transverse-to-the-arc distribution (Pearce et al., 2020).

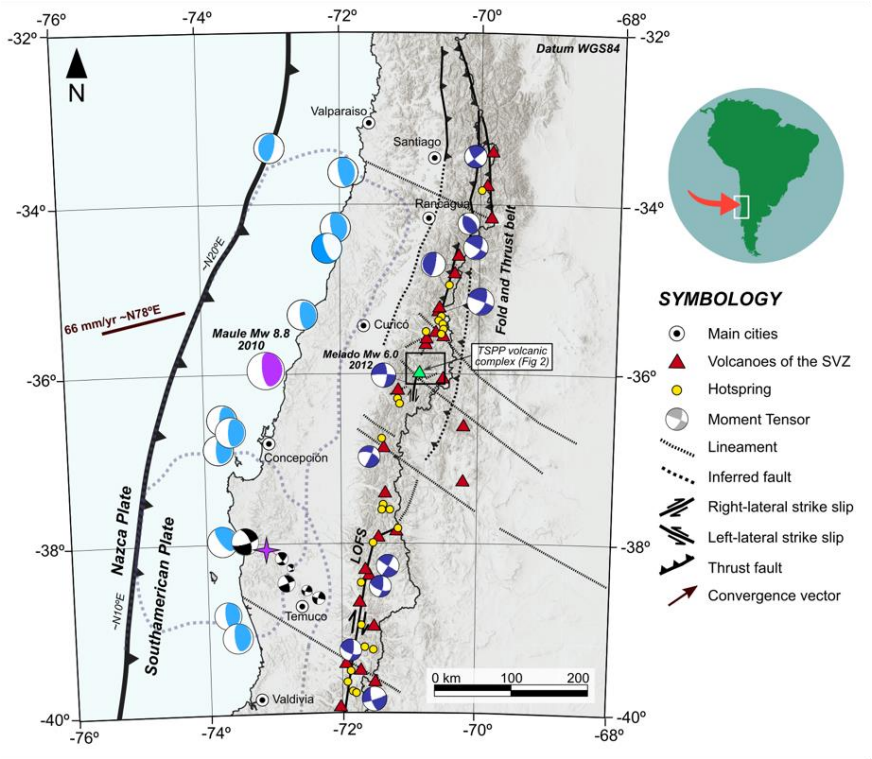

Figure 1: Seismotectonic map of the Southern Andes between 33ºS and 39ºS. Convergence rate and direction are shown by the solid brown vector (Angermann et al., 1999). Rupture zones of the 1960 Valdivia Mw 9.5 and 2010 Maule Mw 8.8 megathrust earthquakes are outlined in lilac dashed lines. Moment tensors of the GCMT catalogue include subduction-type earthquakes (cyan-white beach-balls) and crustal events Mw > 5 and depth <20 km (blue-white beach-balls). Red triangles indicate the location of active volcanoes (taken from the Smithsonian Institute Holocene Volcanic database) and yellow circles indicate the location of geothermal springs (taken from Aravena et al., 2016). Crustal faults systems (LOFS, ATF) and morphotectonic lineaments from Cembrano and Lara (2009) and Pérez-Flores et al. (2016).

At this latitude (36ºS), the Principal Cordillera consists mainly of Mesozoic and Cenozoic volcanoclastic and sedimentary units, as well as Late Mesozoic – Early Cenozoic granitoids (González and Vergara, 1962; Muñoz and Niemeyer, 1984). These units were deformed by regional scale thrusting and folding, with Oligocene – Miocene sedimentary sequences characterized by ~NS-trending asymmetric folds (Sielfeld et al., 2019), whereas Pliocene – Early Pleistocene volcanism is recognized as subhorizontal

pyroclastic layers (Sielfeld et al., 2019b). Sedimentary sequences and granitoids are also intruded by pre-Quaternary dykes that are exposed in the Maule river-Los Cóndores canyon valley.

Active Quaternary volcanism in the study area is represented by the Descabezado Grande volcanic field, Tatara – San Pedro volcanic complex (TSPP), Laguna del Maule volcanic field (LDM), and the Nevados de Longaví volcanic complex (e.g. Stern, 2004) (Figure 2). This constitutes one of the widest segments of the SVZ, up to 60 km wide in the main arc and over 200 km wide in the back-arc region (Stern, 2004). Magnetotelluric surveys in this region show conductive anomalies in the upper crust of the volcanic arc, roughly consistent in location with the TSPP, LDM and Mariposa Geothermal System (MGS) (Reyes-Wagner et al., 2017, Cordell et al., 2018; Hickson et al., 2011).

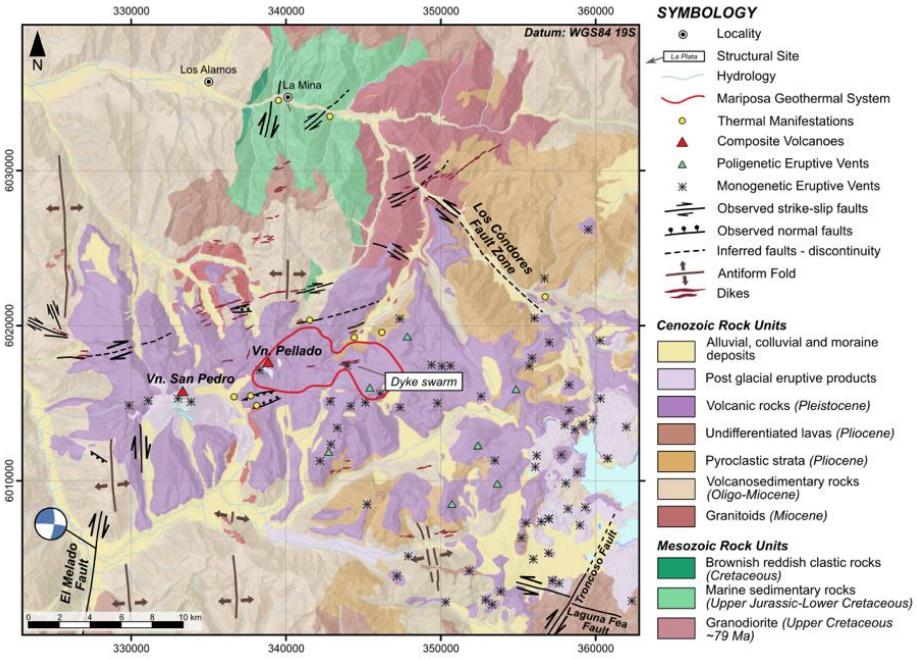

Figure 2: Geological map of the upper Maule river area and the Tatara-San Pedro-Pellado volcanic complex. Distribution of geological rock and sediment units is taken from Hildredth 1997, Singer et al., 1997 (for the detailed stratigraphy). Moment tensor of the 2012 Mw 6.2 crustal earthquake associated to the Melado fault is taken from the GCMT catalogue. Red line indicates the conductive anomaly that represents the Mariposa Geothermal System (Hickson et al., 2011). Location of the studied dyke swarm is indicated.

2.1. Tatara-San Pedro Pellado (TSPP) complex

The TSPP volcanic complex (36ºS) is an ENE trending alignment of two stratovolcanoes (Tatara-San Pedro and Pellado-San Pablo summits from west to east), minor eruptive centres, lava flows, pyroclastic deposits, and dyke swarms that cover an area of over 387 km^2 (Singer et al., 1997). San Pedro volcano is the youngest and most westerly volcanic centre of the complex. Volcanic products erupted from at least three of the central vent regions include both lavas and pyroclastic deposits, and compositionally range from basalts to rhyolites, with mean compositions within the basaltic-andesitic range (ie. 52-56% SiO_2; Davidson et al., 1988; Singer et al., 1997, Dungan et al., 2001; Costa and Singer, 2002). Volcanism in the TSPP commenced at ~925 ka but preserved lavas (~ 54 km^3) represent only a fraction of this time interval (Singer et al., 1997). This implies that either volcanic quiescence, erosional mechanisms such as glacial abrasion, or a combination of both processes have removed significant parts of the eruption record (Singer et al., 1997). Except for small neoglacial moraines, San Pedro volcano is unglaciated, and therefore is of Holocene age (Costa and Singer, 2002).

ENE-striking dyke swarms outcrop in the surroundings of the active San Pedro volcano and cut both pre-eruptive sequences and Pleistocene volcanic units of the TSPP complex (Hickson et al., 2011; Sielfeld et al., 2019; Espinosa, 2019). The dykes vary in composition from andesite to rhyolite, and likely represent parts of the magmatic plumbing system that have fed the TSPP. Singer et al., (1997) mapped abundant ENE-striking dykes in the northern side of the complex. These dykes intrude Pleistocene dacitic lavas of the TSPP through normal faults (Singer et al., 1997). Moreover, Espinosa (2019) mapped ENE to EW-striking and NW-striking dykes to the south of the TSPP.

Sielfeld et al. (2019b) suggest that Quaternary volcanism of the TSPP and the associated MGS have been constructed on top of a ENE-trending damage zone (namely the *Tatara* Damage Zone), a long-lived structural anisotropy of cross-cutting mesoscale ENE-WNW striking transtensional oblique slip faults and dykes, characterized by a graben-like geometry, that has developed before and during the construction of the TSPP.

2.2. Physical Volcanology/Stratigraphy of the TSPP

The TSPP succession has been subdivided into 17 chronostratigraphic units (grouped in 8 sequences described here) based on geologic mapping, geochemistry and

geochronology (K-Ar and ^{40}Ar-^{39}Ar) (Davidson et al., 1988, Singer et al., 1997, Dungan et al., 2001, Costa and Singer, 2002, and Hildreth et al., 2010). From oldest to youngest, these sequences are: (1) Muñoz sequence (925 – 825 ka) composed of a silicic lava dome-flow complex, with phyric lavas and flow breccias, followed by basaltic andesitic and dacitic lavas, and rhyolites. The total preserved volume of the erupted material is 4.8 km^3; (2) Quebrada Turbia (783 – 772 ka) consists of ~1.8 km^3 basaltic andesitic to andesitic lava flows; (3) Estero Molina lavas (605 – 329 ka) composed of ~4.2 km^3 preserved basaltic andesites and rare primitive basaltic flows; (4) Cordón Guadal lavas (512 – 359 ka) consist of basaltic to dacitic lavas; (5) Placeta San Pedro sequence (~230 ka) composed of 2 km^3 of a lower unit of glassy andesitic lava flows with mafic magmatic inclusions and an upper unit made of basalt flows with olivine and clinopyroxene phenocrysts; (6) Pellado volcano sequence (188 – 83 ka) is made of lahars, lavas and pyroclastic rocks ranging in composition from basaltic andesite to andesite with a preserved volume of ~12.5 km^3, that erupted from vents in the vicinity of Cordón San Pablo and Cordón Pellado; (6) Tatara volcano sequence (90 – 19 ka) comprises 22 km^3 of basaltic andesitic to andesitic lava flows, and minor pyroclastic flows; (8) San Pedro volcano sequence (< 10 ka) is the youngest unit. Eruptive activity included early explosive eruptions with pumice, andesitic and dacitic lavas, followed by Strombolian eruptions producing basaltic andesitic scoria and lavas. Part of these lava flows fill a topographic depression generated by the collapse of the early Holocene cone.

3. METHODS

The objectives of this research were addressed through a combination of structural field work, paleo-stress reconstruction and two-dimensional finite element modelling. We took measurements from the well-exposed dyke swarm (0.4 km^2 in area) roughly 5 km to the east of Pellado volcano. Our data complements previous regional scale structural mapping from the surrounding area (Sielfeld et al., 2019b).

3.1. Field methods

Detailed mapping of the dyke segments at the TSPP plateau were conducted to diagnose variations in dyke geometry, mineralogy, attitude and texture. This mapping included

systematic measurement of attitude (strike and dip), thickness and length on each dyke segment. Thickness and segment length were measured directly in the field using a measuring tape when possible. For longer segments, lengths were measured from Unmanned Aerial Vehicle (UAV) images and from a collection of marked GPS points at the start and end of each segment. Where it was not possible to collect field data due to access restrictions, data was recorded from satellite images with a 0.52 m resolution. Sampling of representative dyke outcrops was carried out for further petrographical and fabric analyses at the thin section scale.

3.2. Stress reconstruction: Paleostress analysis from dilatational fracture data

Here we combined the field measurements of dyke attitude with the GArcmB code (http://www.kueps.kyoto-u.ac.jp/~web-bs/tsg/software/GArcmB/) to obtain the stress conditions (orientation of principal stresses and stress ratio) at the time of dyke formation (Faye et al., 2018; Yamaji and Sato, 2011; Jolly and Sanderson, 1997). The code clusters the distribution of poles of dykes (i.e. the vector normal to the dyke plane) by fitting the dataset with a linear combination of Bingham distributions (mixed Bingham distribution), each with its own concentration axes (κ_1, κ_2) and parameters, and interpreted as representing a stress state (Yamaji, 2016; Yamaji and Sato, 2011). Although the method makes a series of assumptions, that are likely a simplification of most natural cases, it provides a first-order approximation of the stress state at the time of dyke formation (the inversion method is further described in Appendix A).

3.3. Finite element method numerical models

We built a suite of plane-strain 2D finite element mechanical models to calculate the static stress field formed around both a volcanic complex and a dyke swarm under different regional loads in order to understand the observed pattern of dyke emplacement. We used the finite-element code ADELI (Hassani et al., 1997), which has previously been used to simulate a variety of geodynamic problems, including long-term deformation at subduction zones (Hassani et al., 1997; Cerpa et al., 2015), interseismic deformation

(Contreras et al., 2016) and volcanic inflation (Novoa et al., 2019). This code uses a time-explicit dynamic relaxation method (Cundall and Board, 1988) to solve the quasi-static equation of motion and has been thoroughly tested through a variety of elastic, visco-elastic and elasto-plastic rheology. In our models here we consider only elastic rheology to determine the conditions that influence the stress field which in turn drives dyke emplacement. More details on the ADELI code can be found in Chéry et al. (2001), Cerpa et al. (2015), Gerbault et al. (2018) and Novoa et al., (2019).

We designed three types of model geometry that simulate 1) the volcanic complex as a sub-circular magmatic-hydrothermal reservoir and pressure source (Model-type 1) (Figure 3a), 2) the dyke swarm as an elongated pressure source on the margins of the complex (Model-type 2) (Figure 3b), and 3) an amalgamation of both geometries with the emplacement of a younger dyke swarm at a greater distance from the complex (Model-type 3) (Figure 3c). Since the modelled domain covers a plane-view section of the tectono-magmatic system at depth, the initial lithostatic equilibrium can be approximated by an initially null stress tensor, hence the effect of gravity is equivalent at constant depth and does not affect the elastic behaviour. All models assume an elastic domain where the crustal section has a density (ρ) of 2750 kg/m^3, a Poisson's ratio (ν) of 0.27 and a Young's modulus (E) of 5 GPa, which are all reasonable values for crustal segments hosting volcanoes (Gudmundsson, 2011, Heap et al., 2020). The specific model geometries are as follows:

- Model type 1: The reservoir is modelled as a circular cavity of radius 1 km. The walls of the cavity are assigned either a magmatic overpressure of 10 MPa or set to a state of lithostatic equilibrium, i.e. the pressure is set to remain equal to zero.

- Model type 2: The active dyke swarm is modelled as an elliptical cavity with a length of 1 km and a thickness of 150 m (diameter of long and short axes). A magmatic overpressure of 10 MPa was applied to all of the walls of the cavity.

- Model type 3: The chilled dyke swarm is modelled as a meshed ellipse with a stiffness (Young's moduli) of 50 GPa, i.e. 5 times higher than the rest of the modelled domain.

The crustal properties are kept constant throughout all of the model simulations. The size of the magmatic-hydrothermal reservoir is constrained by the shape of conductive bodies

obtained from a magnetotelluric profile (Reyes-Wagner et al., 2017), while the orientation of dykes was measured directly in the field. The lengths of the dykes in the models are deliberately one order of magnitude larger than measured in the field for purposes of mesh resolution. As we assume plane-strain deformation the model is symmetrical in the third, vertical dimension, hence the cavities and ellipses are cylindrical features, similar to previous assumptions such as by Gudmundsson and Andrew, (2007), Andrew and Gudmundsson (2008), Gerbault et al., (2012).

The model geometries are meshed with the *Gmsh* software (http://gmsh.info/)_using tetrahedral elements (the third dimension is meshed to a thickness of 0.75 km but plane-strain conditions leads to effectively 2D models). The mesh resolution is highest in areas near the cavity boundaries. The total number of elements is in the order of tens of thousands and slightly varies from one model to the other.

All of the three model geometries are loaded using two different boundary conditions. They are as follows and shown schematically in Figure 3 (d, e):

1. Loading condition 1: Internal magmatic excess pressure of 10 MPa applied to the boundaries of both the circular reservoir and elongated dyke, in order to simulate fluid overpressure. As we assume that each cavity is filled with melt, the tangential stress at the cavity boundaries is zero. The other boundaries of the model are set free slip, i.e. they are only fixed in their normal direction (i.e. avoiding rigid body rotation) (Figure 3d).
2. Loading condition 2: A combination of internal magmatic excess pressure of 10 MPa applied on the boundaries of the reservoir and dykes, and a horizontal compression (Sx) of 1 MPa is applied at the horizontal boundaries of the model domain (X direction, mimicking E-W compression). This horizontal compression is applied as a velocity normal to the vertical borders, so that the total displacement (shortening) at the end of the model run reaches Dx~4.3 m. With free-slip horizontal borders, this loading condition builds uniaxial strain, and yields a background stress state of 1 MPa within the homogeneous domain.

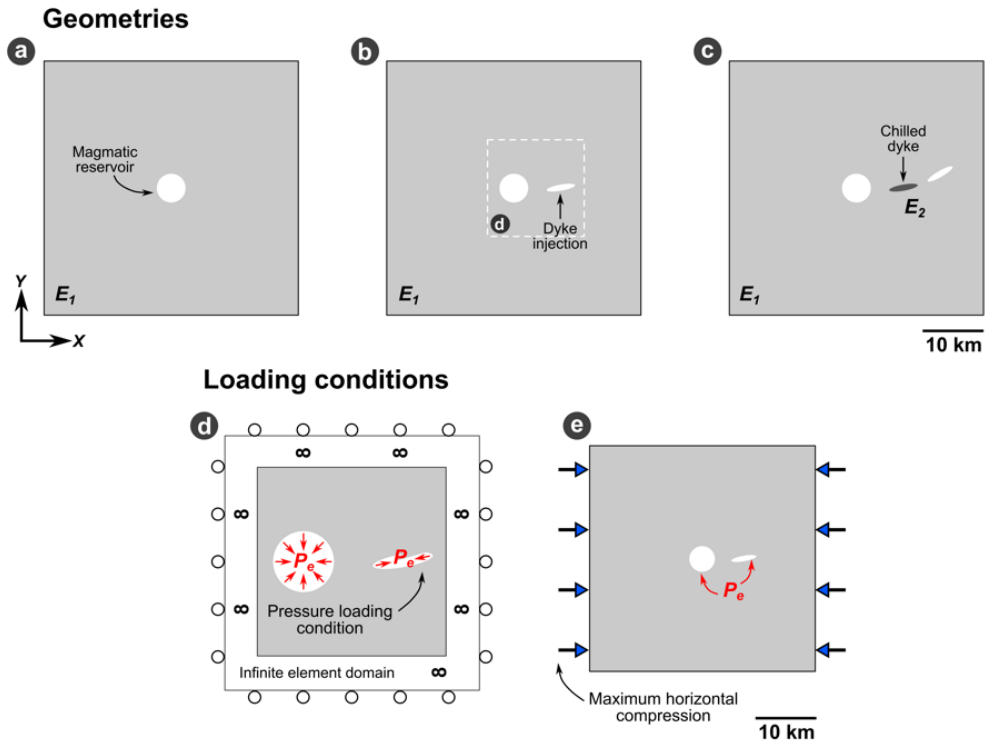

Figure 3: Models setups, assuming horizontal plane strain conditions. (a) The magmatic/hydrothermal reservoir is modelled as a circular cavity of 1 km radius embedded in the centre of the elastic domain. (b) Dyke injections are modelled as elliptical cavities, while (c) chilled dykes are modelled as ellipses with mechanical properties different to that of the host rock. The loading conditions simulated are (d) an internal magmatic excess pressure in the reservoir and dyke, (e) a combination of both pressure in the cavities and regional compression. In the simulations using the loading conditions given in model (d), the X and Y normal boundaries are free slip surfaces that are held stationary in their normal directions (dyke geometries are not to scale).

4. RESULTS

We now present results from all of the three types of analyses that were carried out: field observations (4.1), paleo-stress reconstructions (4.2), and the numerical modelling (4.3). The results are further synthetized together in section 5.

4.1. Field Observations and Analyses

The dykes are exposed over a narrow area (approximately 400 m in width and 1 km in length) (Figure 4; Figure 5a) and cross cut 103 ka old lavas of the Pellado volcano stratigraphic sequence (Singer et al., 1997). To the south of the dyke swarm exposure extends a plateau at ~2500 m.a.s.l. where eroded lava flows and scoria of various hues crop out outcrop. Some dyke segments of the swarm outcrop to the north yet are

inaccessible due to steep-sided slopes. Dyke segments were easily identified because they rise sharply over the eroded basaltic lavas which they intrude.

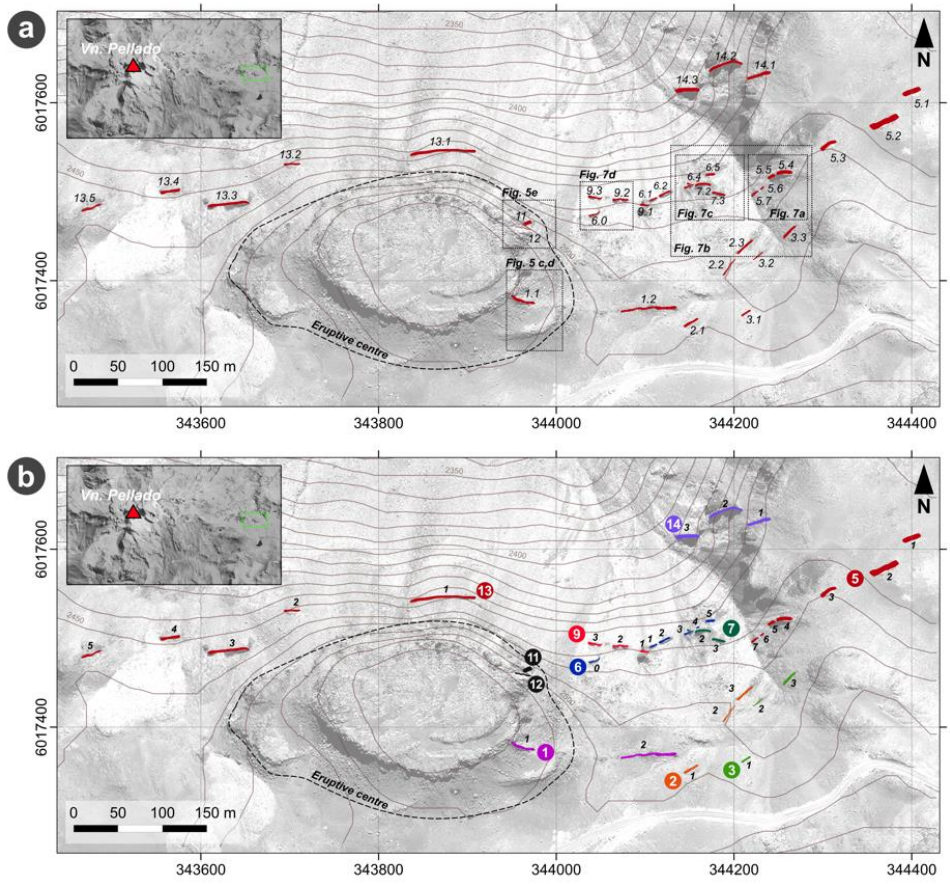

Figure 4: Map of the studied dyke swarm. Inset image indicates the location of swarm (green box) relative to the Pellado volcano. Dyke segment is indicated with a number in the image (Dyke ID – segment). (b) Interpretative map of the studied dyke swarm. Colours indicate to which "total dyke length" each segment is associated to. Inset image indicates the location of swarm (green box) relative to the Pellado volcano. Numbers indicate the dyke segment ID.

In the central part of the dyke swarm we observe the remnants of a steep-sided scoria cone of approximately 358 m length and 175 m width (Figure 5b). The cone is made of distinct units of multidirectional jointed lavas, topped by near-horizontal units of scoria (Figure 5c). On the upper most surface of the cone we observe glacial striations trending ENE and NNW (Figure 5b). Within a section of wall of the eastern most side of the cone we observed three dyke segments. One of the dykes is ~5 m-thick and transitions into a

lava feeder near the surface of the cone (Figure 5d). The other two dyke segments are ~1 m in thickness and are arrested within the cone, making it possible to identify their tips. These segments did not feed an eruption (Figure 5e).

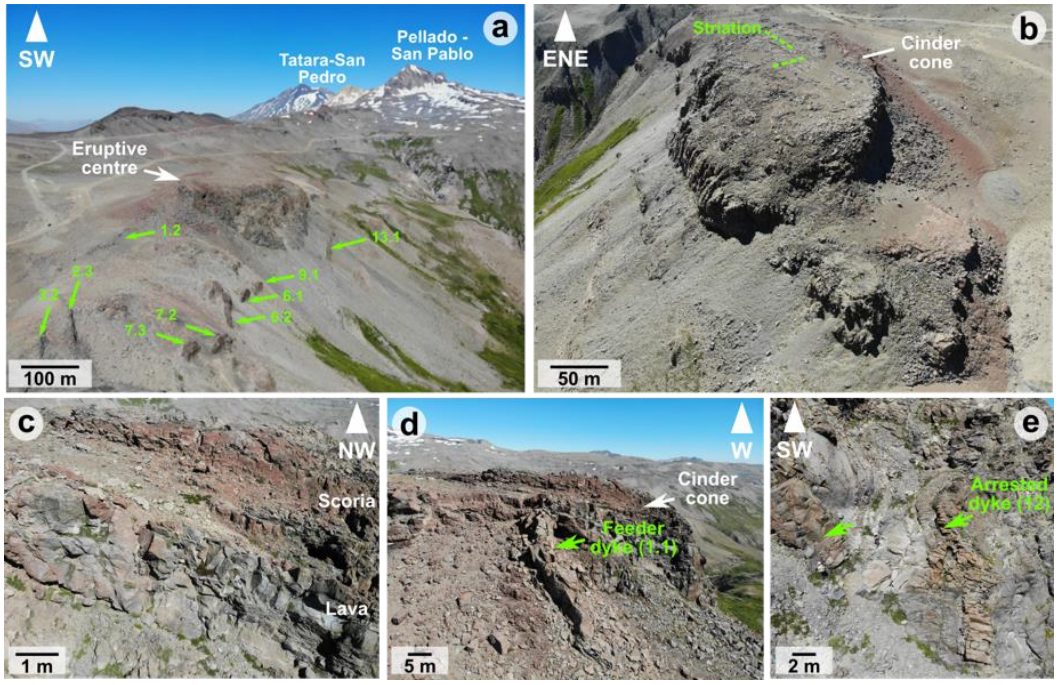

Figure 5: Drone images of the dyke swarm. (a) View of the volcanic complex summits in the background, the cinder cone (or mafic mound) and dykes (indicated with green arrows); (b) Top down photograph of the cinder cone (mafic mound). The green segmented lines indicate the two preferential directions of striation (NNW and ENE striking). To the N of the cinder cone, we can observe dyke segment 13.1; (c) Uppermost segment of the cinder cone showing a level of scoria overlying near horizontal levels of basaltic jointed lavas; (d) Lateral view of the cinder cone (mafic mound) and the feeder dyke; (e) Lateral view of the cinder cone and the two arrested dykes.

In total, we measured 35 dyke segments which range in thickness from 0.56 m to and 7.15 m (Table 1) (Figure 6). The total length of the dyke swarm is ~1 km, but individual dyke segments range in length between 4.3 m to 60.6 m (Figure 6). In the field it was not possible to identify dyke tips, in their lateral extensions, and therefore we do not rule out the possibility that these dyke lengths are underestimated. Based on the orientation, thickness and mineralogy we interpret that the 35 segments belong to only nine dykes, each comprised of between 2 and 5 segments. This results in total outcropping dyke lengths between 40 m and 170 m (Figure 4b). Each dyke is distinguished with a number in Table 1 and Figure 4. The segment of each dyke is also recorded.

Table 1: Dyke segment parameters as measured in the field, from UAV images and from a collection of marked GPS points. Dykes are identified by two numbers: the first indicates dyke number and the second indicates the segment number. Last column indicates the aspect ratio of 33 dyke segments. (*) Dykes are exposed in a vertical section, thus length is not an observable feature.

Segment	Strike (RHR)	Thickness (m)	Length (m)	Aspect Ratio (w/L)
1.1	291	3.70	28.05	0.13
1.2	89	1.59	55.15	0.03
2.1	250	2.40	14.42	0.17
2.2	25	1.80	20.00	0.09
2.3	35	1.30	12.81	0.10
3.1	68	2.75	7.28	0.38
3.2	54	1.33	13.42	0.10
3.3	58	2.40	19.50	0.12
5.1	87	7.15	17.46	0.41
5.2	55	6.70	25.94	0.26
5.3	60	3.90	25.00	0.16
5.4	220	5.50	18.08	0.30
5.5	39	3.20	9.41	0.34
5.6	55	2.16	17.54	0.12
6.0	47	2.50	11.05	0.23
6.1	260	3.23	26.45	0.12
6.2	57	1.90	8.92	0.21
6.3	68	1.70	4.30	0.40
6.4	78	2.71	6.74	0.40
7.1	233	3.23	17.42	0.19
7.2	263	3.05	6.83	0.45
7.3	105	2.07	14.11	0.15
9.1	105	2.40	7.62	0.31
9.2	90	5.60	18.20	0.31
9.3	101	3.23	15.64	0.21
11.1	73	5.16	(*)	(*)
12.1	140	0.56	(*)	(*)
13.1	94	2.25	60.66	0.04
13.2	91	2.51	13.14	0.19
13.3	84	3.55	46.93	0.08
13.4	85	3.51	23.71	0.15
13.5	71	2.00	24.70	0.08
14.1	77	2.81	21.37	0.13
14.2	69	2.76	41.49	0.07
14.3	87	3.07	23.36	0.13

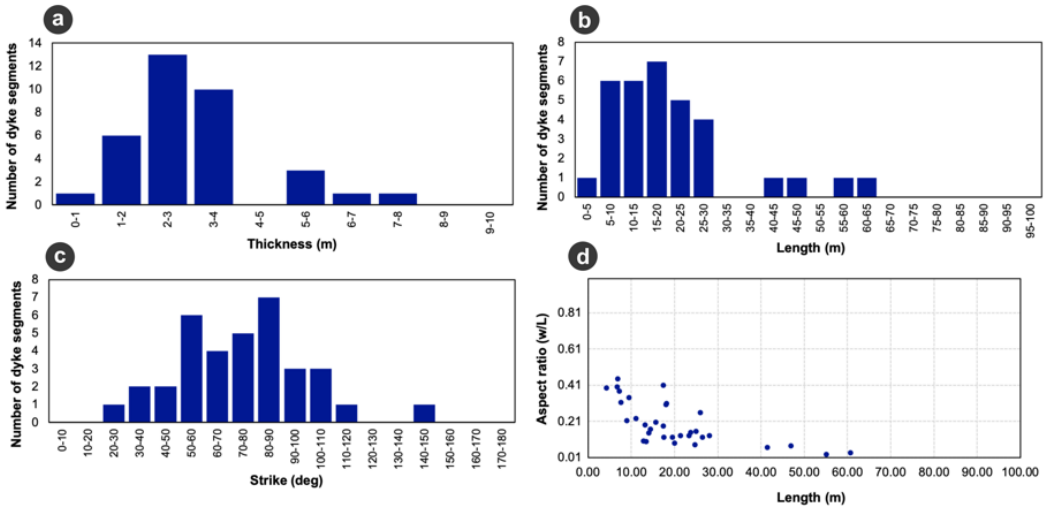

406

407 **Figure 6: Histogram showing the distribution of 33 dyke (a) thickness measured; (b) dyke**
408 **segment length; (c) strike; (d) logarithmic scale plot of aspect ratio vs. dyke segment**
409 **length.**

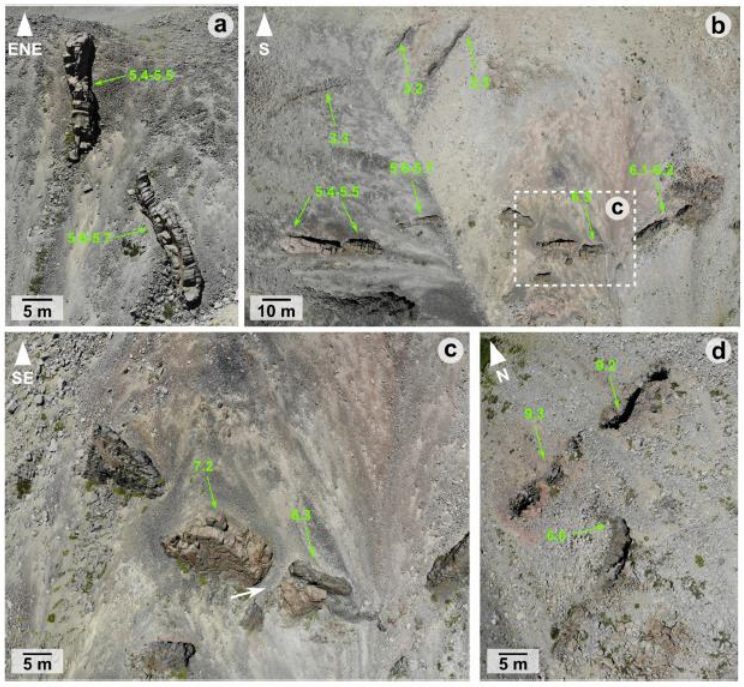

410

411 **Figure 7: Drone images of the dyke swarm. (a) Near-vertical and near-strike view of two**
412 **dyke segments of ~5 m thickness; (b) Near-plan view of segments in the dyke swarm. It is**
413 **possible to observer ~20º rotations of dyke segments (ie. green arrow); (c) Lateral view of**
414 **cross-cutting dykes; (d) Rotation of nearly ~20º of a dyke segment.**

415

416 The dyke segments exposed in the area all dip steeply between ~70 – 90º, and strike
417 predominantly between N50ºE and N90ºE, with some segments striking WNW (n=8)

(Figure 6). We can distinguish two preferential orientations at N50º-70ºE (n=10) and N70º-90ºE (n=12) indicating an apparent rotation in strike orientation of about 20º. The distance over which segmentation and changes in strike orientation occur, are within the same order of magnitude as the dyke thickness, i.e. cm to m. Such changes also relate to dyke segments with similar textures and mineralogy (Figure 7b, d). Poor cross-cutting relations between these predominant orientations suggests that the N50º-60ºE striking dykes are younger than the E-W-striking dykes (Figure 7c). There does not appear to be a clear en-échelon segmentation of the dyke segments but the ~20º rotation in strike orientation of the dyke segments could reflect an incipient en-échelon pattern.

The composition of all the dykes is porphyric basalts with a plagioclase, clinopyroxene and orthopyroxene phenocrystic phase and small amounts of olivine in a crypto crystalline groundmass of plagioclase, pyroxenes and glass. We did not observe evidence of more evolved magmatic compositions in the swarm. In some samples, micro plagioclase crystals in the groundmass show a preferred orientation, parallel to the dyke's edge. Most samples possess vesicles but only one dyke exhibited vesicles elongated parallel to the margin. Moreover, some dyke segments (5.1 – 5.5) have a ~40 cm chilled margin and brecciated clastic edges, with clast size of 2 – 6 cm. They also display quench textures in the border, indicative of rapid cooling. There is no clear breccia texture between the ~40 cm margin and the centre of the dyke, but a smooth textural transition.

4.2. Paleo Stress Reconstruction

To reconstruct the paleo stress conditions during dyke emplacement we performed an inversion from the orientation (strike and dip) of 35 dyke segments. The data set shows an optimal K value of 1, meaning that one single stress condition can be used to explain the orientation of all the dyke segments. This stress state corresponds to a stress regime with a horizontal NW-trending σ_3 (336º/0.4º), a horizontal NE-trending σ_2 (066º/0.8º), and a vertical σ_1 (219º/89.1º). The resulting stress shape ratio is Φ=0.1, indicating that $\sigma_2 \approx \sigma_3$ (Figure 8).

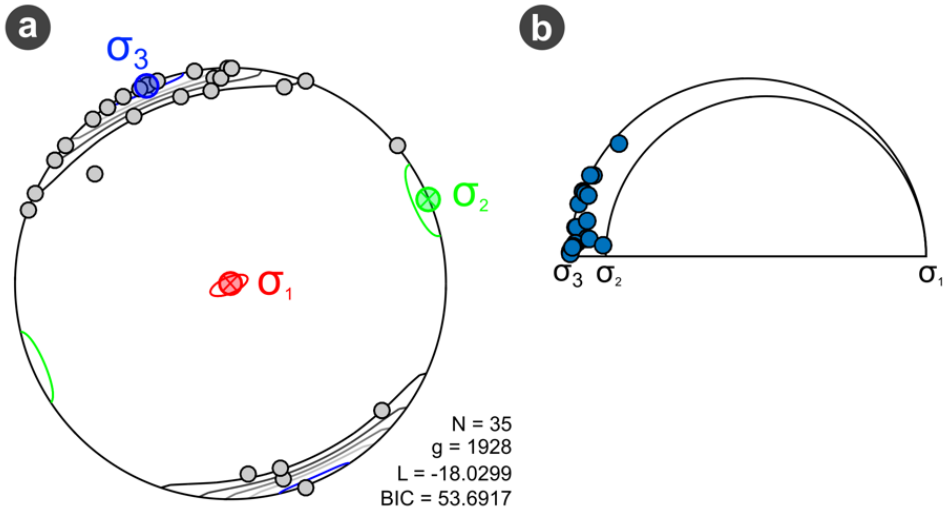

Figure 8: Results of the inversion of dyke orientation data (n=35) (a) Lower-hemisphere equal-area projection includes pole to dyke-planes as grey circles and paleo stress tensor orientation; (b) Mohr diagram resulting from the stress inversion. Magnitude of σ_2 and σ_3 are similar.

4.3. Model Results

A total of 12 numerical models were run by varying the geometrical setups and loading conditions which we briefly summarize again here for clarity. Model type 1 simulates the stresses situated around an inflating reservoir of radius 1 km. This first model type is used to inform the second two model types by comparing the orientation of the resulting principal stresses with the dyke orientations observed in the field. The second model type (Model type 2) builds on model type 1 by adding an elliptical cavity, which simulates a dyke emplaced in a region consistent with the dyke swarm observed in the field. The third model type (Model type 3) builds on both model types 1 and 2 by introducing a stiff inclusion, that simulates a chilled dyke, and which is set in between the pressurized cylindrical cavity and a more recently emplaced elliptical dyke segment.

All of the three model types were subjected to the two loading conditions discussed previously. Here we discuss the results after applying (1) 10 MPa of excess pressure only along the cavity boundaries, and (2) applying both 10 MPa excess pressure along the cavity boundaries and a 1 MPa E-W compression applied from the model edges.

To examine possible propagation paths and interactions between dykes, we focus on the magnitude of the least compressive principal stress (σ_3; hereafter referred to as σ_h), or tensile stress, and the orientation of the most compressive principal stress (σ_1; hereafter referred to as σ_H). Further below we will *abusively* use these notations,. We also display the volumetric strain, which is the first invariant of the strain tensor and expresses its isotropic component (as I1 in the figures). Through analysis of principal stresses and volumetric strain, zones of both contraction and dilation can be discerned.

4.3.1. Model-type 1: circular cavity

In Figure 9 we show the results of the numerical simulations using the geometry of Model type 1 and the two end-member loading conditions. In loading condition 1, with only the application of an excess pressure of 10MPa from the circular cavity walls, the tensile stress (σ_h) decreases radially from a maximum value of 10 MPa at the walls of the cavity to almost zero in areas >2 km away. The orientation of σ_H σ_1 trajectories is radial (Figure 9a). These results reproduce analytical solutions in which for plane-strain, the stress field decays as $1/R^2$ (e.g. Timoshenko & Goodier, 1970, e.g. see also benchmarks in Gerbault et al., 2012).

Figure 9 (c, d) shows the result of loading the same geometry with an overpressure in the circular cavity and an E-W compression of 1 MPa (loading condition 2). The effect is an overall increase in the magnitude of σ_3 the least compressive stress in the bedrock, decreasing from a maximum value of >25 MPa at the cavity walls to ~1 MPa in areas away from the cavities. The trajectories of the σ_1 still rotate around the circular cavity as in the model with loading condition type 1, but now align more closely along the orientation of the applied horizontal compression in areas away from the cavity (Figure 9c). Zones of contraction and dilation develop to the north-south and east-west of the cavity respectively (Figure 9d), with volumetric strain decaying away from the cavity walls.

These results indicate that regions to the east-west of the cavity would favour magma propagation through dykes striking ENE and WNW at locations close to the cavity (~2 km) and striking E-W at locations further away from the cavity (>2 km). Regions to the north and south of the cavity undergo uniform compression, and also exhibit unfavourable orientations of σ_1, thus dyke propagation would be inhibited to the north and south of the magmatic cavity. These results are in agreement with classic mechanical studies by Griffiths (1924) (among others) and recent experimental results obtained by Li et al. (2017) for marble specimens with circular holes, where the formation of tensile cracks occurs in the loading direction due to the increase of micro crack density.

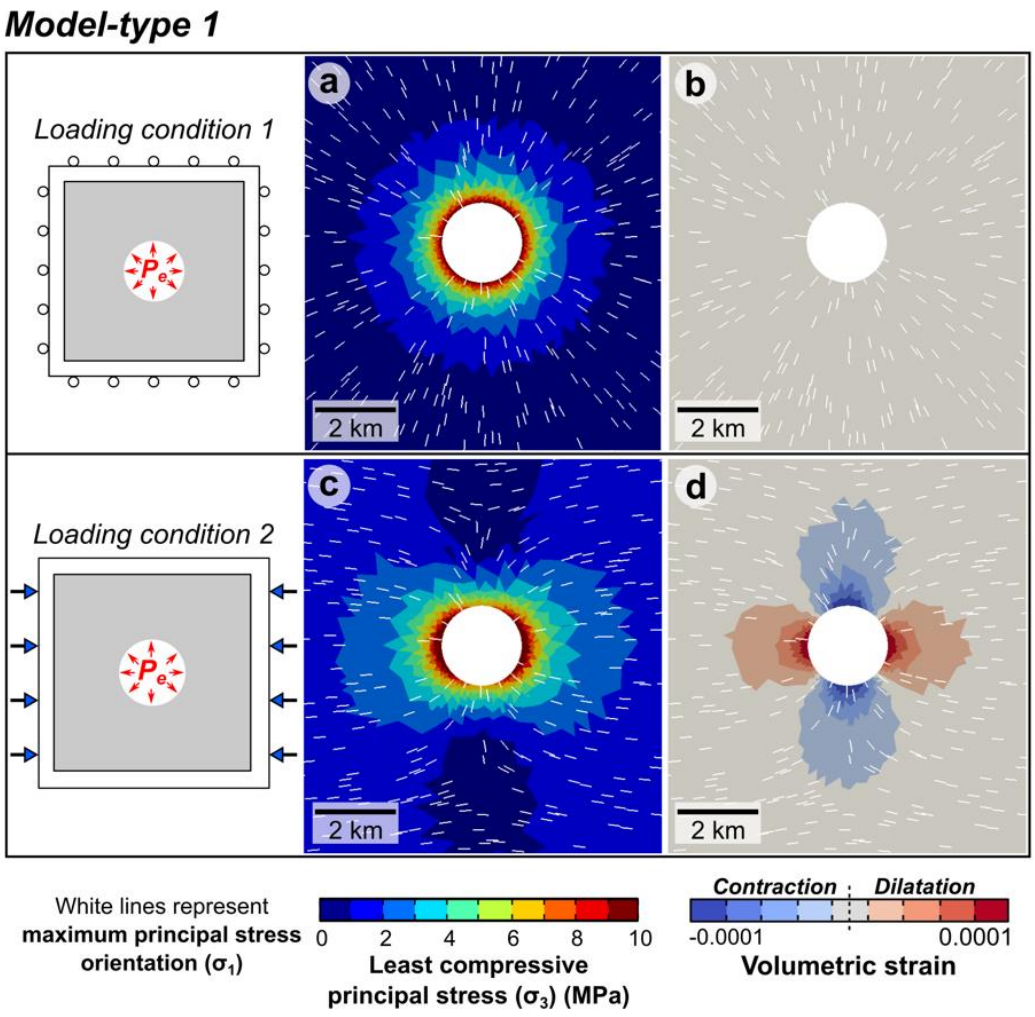

Figure 9: Model results of a pressurized circular cavity (Model-type 1) considering two loading conditions. (a) and (b) provide model results when applying loading condition 1, (c) and (d) show model results when applying loading condition 2. (a) Magnitude and distribution of least compressive principal stress displayed with the orientation of the maximum principal stress trajectories, (b) Volumetric strain. (c) σ_1 stress trajectories. σ_H rotate when a far-field compressive load is applied, showing that a far field stress field exerts an important control on regional dyke swarms. (d) Volumetric strain. The bedrock undergoes contractional strain to the north and south of the circular cavity and dilatational strain to the east and west.

4.3.2. Model-type 2: elliptical cavity

Figure 10 shows the results of the model geometry that considers a plane-view section of both the volcanic complex and a nearby radial dyke swarm striking N80ºE (Model-type 2). This model-type represents the first stage of a dyke swarm injection as discerned from the field measurements. When an excess pressure of 10 MPa is applied in both the

circular and elliptical cavities, the stress field develops and decays away from these cavities. Tensile stress (σ_3) concentrates at the tips of the dyke swarm (Figure 10a), as well as dilatational strain (Figure 10b). In contrast along the elongated sides of the dyke swarm we note contractional strain. The trajectories of σ_1 are distributed radially around the circular and elliptical cavity; particularly, at the tip of the dyke they are oriented parallel to the direction of the major semi-axis of the dyke, while along its long edges, the trajectories are oriented perpendicular. This is in agreement with the volumetric strain pattern.

Figure 10 (c, d) shows the result from loading the same geometrical configuration with loading condition 2 (e.g. applied cavity overpressure plus lateral compression). The region located in between the inflating cavities experiences a larger amount of tensile stress and hence dilatational strain (Figure 10 c, d). The σ_3 stress contour of 2-3 MPa links both cavities. The trajectories of σ_1 rotate to a near EW orientation at the east of the dyke tip. Ahead of the dyke tip, the trajectories of σ_1 strike within +/- ~13° to the orientation of the dyke strike, rotating within 4º to 20º (clockwise and anticlockwise rotations) with respect to the trajectories of σ_1 obtained with loading condition 1. Within 1.5-2 km (~dyke length) to the north and south of the dyke, trajectories of σ_1 rotate by 7º to 30º (clockwise and anti-clockwise), while areas further away than 2 km, they rotate by up to +/-75º compared to the trajectories of σ_H obtained with loading condition 1, as they align more closely to the loading direction.

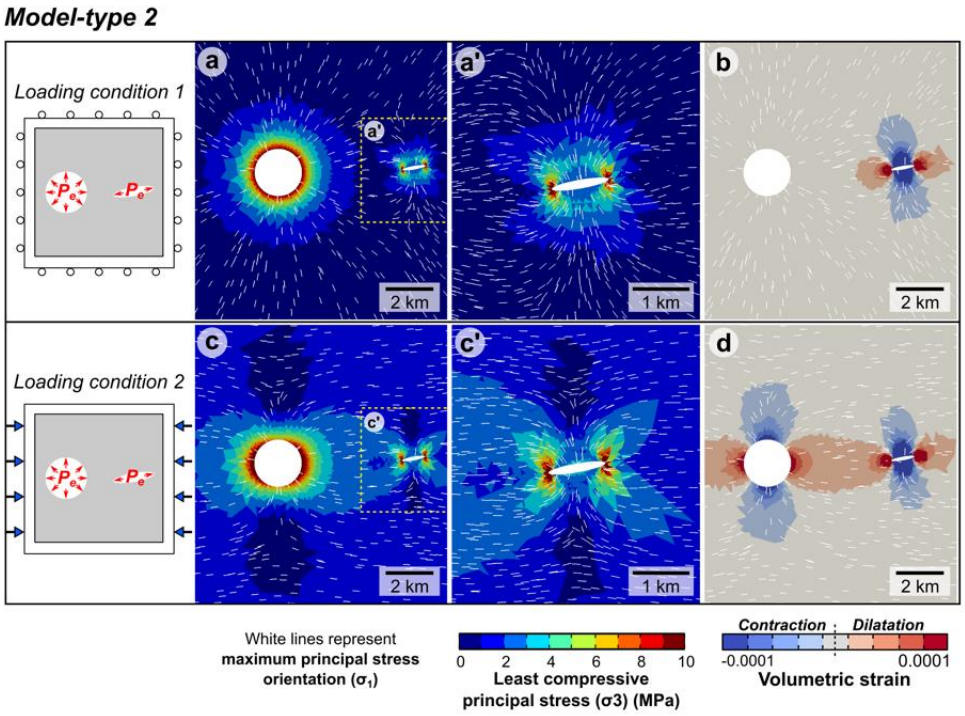

Figure 10: Model-type 2 considering two loading conditions. (a) and (b) present results when applying loading condition 1, (c) and (d) show results when applying loading condition 2. (a) Least and most compressive stresses (σ_3 and σ_1 respectively), colour contour and trajectories. Both magnitude and trajectories decay radially around the circular cavity, while around the dyke, stress concentrates at the tips. (b) Volumetric strain. The bedrock to the WSW and ENE of the dyke undergoes dilatational strain. (c) σ_3 colour contour and σ_1 trajectories. The magnitude of σ_3 increases in the bedrock compared to loading condition 1; σ_1 trajectories align to the loading direction (d) Volumetric strain. A region undergoing dilatational strain links both cavities, as well as to the ENE of the dyke.

4.3.3. Model-type 3: elliptical cavity and stiff inclusion

Figure 11 shows the results of a model geometry that considers together the volcanic complex, a cooled or stiff dyke swarm, and a new radial swarm striking N60ºE (Model-type 3). Now, the dyke that was used in Model-type 2, is modelled as a stiff inclusion, i.e. a unit with a Young's modulus five times that of the host-rock (50 GPa). A second elliptical cavity striking N60ºE is added to the east of the previous dyke (strike N60ºE), simulating a later dyke injection.

When applying an over pressure of 10 MPa (loading condition 1, Figure 11 a, c) to both the circular and second elliptical cavity boundaries, the stiff dyke has the effect of

increasing the magnitude of the tensile stress (σ_3) at the closest dyke tip, i.e the westernmost area of the pressurised dyke. The bedrock in this area also undergoes dilatation. On the other hand, the magnitude of σ_3 in the bedrock to the east of the easternmost dyke tip is less, most likely due to its broader distance from the circular cavity compared to the westernmost dyke tip. This broader distance also inhibits linkage between the two over-pressured cavities. σ_1 trajectories in the region between the inflating cavities strike ENE, and in the region east of the easternmost inflating dyke tip, the trajectories strike NE.

The influence of the stiff dyke becomes more pronounced when applying loading condition 2. In this case the stiff dyke acts partly as a stress barrier to the σ_3 stress generated by the new pressurized dyke (Figure 11c). The region located in between the inflating cavities and the tips of the inflating dyke experiences dilatational strain, still without interacting much (Figure 11 c, d). The regions to the NW/SE of the inflating dyke undergo contractional strain. The trajectories of σ_1 in the region between the inflating cavities are ENE to EW striking, rotating slightly (up to 15º) with respect to σ_1 trajectories obtained from loading condition 1. In the region east of the easternmost inflating dyke tip they rotate by 7º to 24º with respect to σ_1 trajectories obtained from loading condition 1, from predominantly NE striking to ENE striking trajectories, as again, they align more closely to the loading direction.

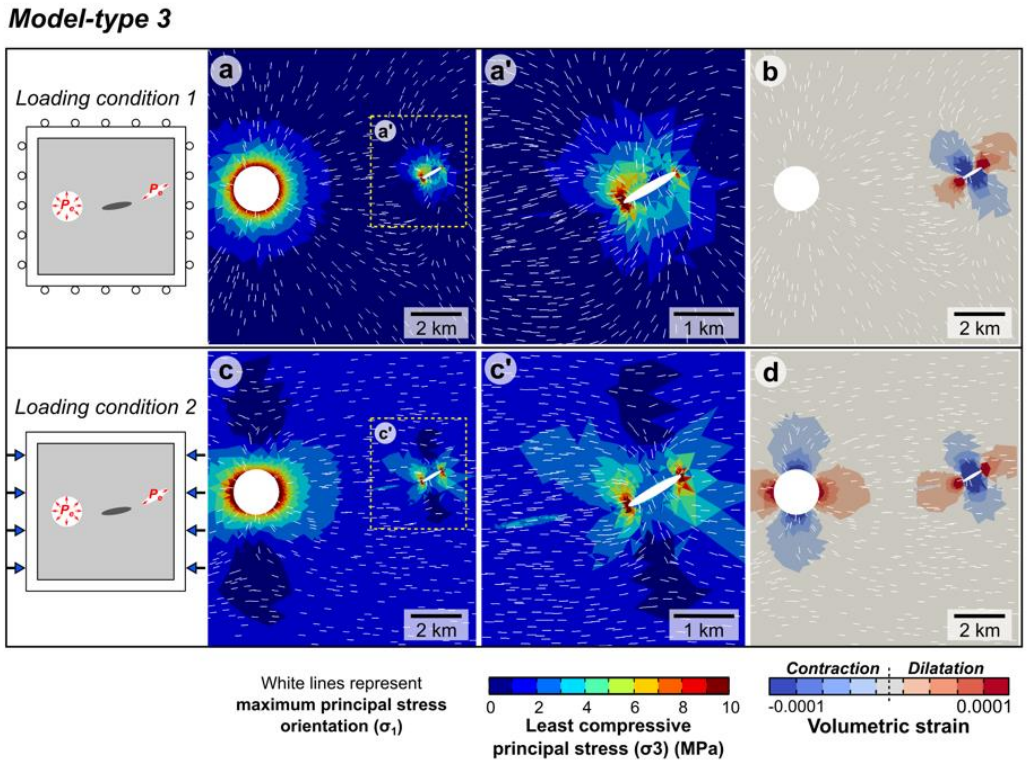

Figure 11: Model-type 3 considering two loading conditions. (a) and (b) correspond to the model results when applying loading condition 1, (c) and (d) show the model results when applying loading condition 2. The stiff dyke has Young's modulus equal to 50 GPa. (a) Least and greatest principal stresses (σ_3 and σ_1 respectively), colour contour and trajectories. Tensile stress concentrates at the pressurized dyke tips and is intensified at the westernmost dyke tip. (b) Volumetric strain. The bedrock to the WSW and ENE of the pressurized dyke undergoes dilatational strain. (c) Contour plot of the σ_3 and σ_1 trajectories. The magnitude of σ_3 increases in the bedrock compared to case (a). The stiff chilled dyke acts as a stress raiser (concentrator), where σ_3 reaches ~4 MPa. (d) Volumetric strain. The chilled dyke undergoes constriction while the surroundings undergo greater dilatational strain than in case d) (by ~0.00002).

5. DISCUSSION

In this section, we integrate all of field observations, paleo-stress analysis and numerical models to consider the emplacement of a dyke swarm of the to the East of Pellado volcano, TSPP volcanic complex. Our field observations indicate that the observed section of the dyke swarm was likely emplaced at very shallow depths and contributed to feeding a series of fissure eruptions. Our numerical models indicate that the orientation of principal stresses can rotate in the presence of previous dyke injections, which is due in part to the geometry of the dykes interacting with both local and far-field loading

598 sources. These results are discussed and interpreted following four main topics to
599 facilitate their understanding: (1) the dyke segment geometries; (2) the temporal evolution
600 of the dyke swarm and the role of previous dykes in influencing propagation paths; (3)
601 estimation of reservoir conditions from the dyke geometry; and (4) a conceptual model
602 and regional implications associated with dyke emplacement .

603 **5.1. Dyke segment geometry and evidences of a dyke-fed subglacial eruption**

604 The 35 dyke segments studied here, form a ~ 1 km long swarm that fed a sub-areal or
605 sub-glacial eruption. This is indicated by a feeder dyke that transitions into a lava feeder
606 near the surface of a ~358 x 175 m eruptive cone. Striations in lavas at the top of the
607 eruptive cone could be related to glacial erosion (Singer et al., 1997.

608 The measured thickness of the feeder dyke (> 4 m) is similar to that of other typical feeder
609 dyke thicknesses measured, for example by Geshi et al. (2010; 2020) in the caldera walls
610 of Miyakejima volcano. The thickest segments measured in the swarm have maximum
611 lengths < 26 m, while the longest segments (L > 50 m) are no more than 3.5 m thick. The
612 thickness: length aspect ratio of individual segments ranges between 0.03 and 0.45
613 (mean and median of 0.20 and 0.16 respectively), values that are abnormally high for
614 dykes, which generally have thicknesses: length aspect ratios in the range of 10^{-2} and 10^{-4}
615 (Rubin, 1995). However, when we consider the entire dyke lengths rather than individual
616 segments, the aspect ratio falls much closer to this range, with ratios between 0.016 and
617 0.090 (mean and median of ~0.04). This highlights the importance of considering, where
618 possible, full dyke lengths rather than dyke segments which may lead to erroneous
619 interpretations (e.g. Daniels et al., 2012).

620 However, dyke segmentation as observed in the studied swarm is a common and inherent
621 feature in dykes, that occurs due to lateral variations in crustal stresses, decreasing
622 overpressure, crustal discontinuities, variable in-situ tensile strength and/or rock layering
623 (e.g., Delaney and Pollard 1981; Baer and Beyth 1990; Gudmundsson, 2020). Therefore,
624 it should be assumed that the dyke segments are connected to a deeper parent dyke and
625 are hence continuous at some greater depth below the surface. We hypothesize that this
626 dyke swarm reached near-surface crustal levels and generated an eruption, therefore
627 segmentations could have occurred due to decreases in overpressure when reaching the

surface or simply through changes in the crustal properties at shallow depths. The changes in strike observed in the exposed dyke segments result from a rotation of the stress field around a vertical axis (usually assumed to be parallel to the propagation direction), yet the expected en-échelon pattern is not clearly observed.

Based on Hoek's classification of dyke-fracture geometry (1991), the exposed dykes can be described as a combination of both irregular and braided patterns. The dykes present little or no overlap between segments and occur in offsets, both characteristic of irregular segmented fracture systems. The dykes in the swarm are also characterized by the side-by-side occurrence of segments that defines braided dykes (Hoek, 1991).

5.2. Overpressures and depth of magma chamber of the feeder dyke swarm

Aspect ratios (thickness: length) of the dykes were used as input to analytically estimate the magmatic overpressure p_o and depth to the dyke source (h) of this feeder dyke system. We thus undertake the methodology adopted by e.g. Gudmundsson (2011); Becerril et al. (2013), as a first order insight on the depth source of our dyke systems. The aspect ratio of a dyke (w/L) is related to its internal fluid overpressure (p_0) and elastic parameters (E, ν) by equation (1). Moreover, p_0 is also related to the magma's buoyancy $(\rho_r - \rho_m)$, (where ρ_r and ρ_m are the host rock and magma densities), the fluid excess pressure in the source (p_e) (in excess of the lithostatic stress), the differential stress state at the surface (σ_d) and the depth to source (h) by equation (2).

$$w = \frac{2p_0(1-\nu^2)L}{E} \tag{1}$$

$$p_0 = p_e + (\rho_r - \rho_m)gh + \sigma_d \tag{2}$$

From the first equation, we can calculate p_o, and by combining equations (1) and (2) we can estimate the depth to source as follows:

$$h = \frac{p_0 - p_e - \sigma_d}{(\rho_r - \rho_m)g} = \frac{wE}{2L(1-\nu^2)(\rho_r - \rho_m)g} - \frac{(p_e - \sigma_d)}{(\rho_r - \rho_m)g} \tag{3}$$

Table 2 shows the resulting overpressure and depth of origin of magmas for 9 dykes, obtained by assuming constant standard values for p_e and σ_d (2.5 and 1 MPa respectively). We are aware that there could exist uncertainty in these values that could thus affect our estimations. Nevertheless, using the aspect ratios of "total dykes" (0.016 – 0.09), we estimate magmatic overpressures to range between 8.7 and 28.7 MPa. The calculated overpressures are similar to those obtained from dyke aspect ratios in other regions and numerical models from Laguna del Maule (e.g. Geshi et al., 2010; Gudmundsson, 2011; Becerril et al., 2013, Novoa et al., 2019; Geshi et al., 2020), and could be associated to mid crustal reservoirs. The estimated depths to the source reservoir of the dykes range between 2.7 and 22.8 km.

Table 2: Magmatic overpressure and depth of origin of magmas for 9 total length dykes. Constant values used for these calculations are the following: Young's modulus (E) and Poisson's ratio (ν) of the host rock is 1 GPa and 0.25 respectively; the average density of the host rock (ρ_r) and magma (ρ_m) is 2650 kg/m^3 and 2450 kg/m^3 respectively; internal excess magmatic pressure in the reservoir (p_e) is 2,5 MPa; differential stress (σ_d) is 1 MPa; and acceleration due to gravity (g) is 9,81 m/s^2. (*) Thickness is taken as the arithmetic mean of dyke segment thickness; (**) Total length is taken as the sum of dyke segment lengths.

Dyke	Thickness (m) (*)	Total Length (m) (**)	Aspect ratio (T/L)	Overpressure (MPa)	Depth (km)
1	2.6	83.2	0.03	17.0	6.9
2	1.8	47.2	0.04	20.7	8.8
3	2.2	40.2	0.05	28.7	12.8
5	4.8	113.4	0.04	22.4	9.6
6	2.4	57.5	0.04	22.4	9.6
7	2.8	38.4	0.07	38.7	17.9
9	3.7	41.5	0.09	48.2	22.8
13	2.8	169.1	0.02	8.7	2.7
14	2.9	86.2	0.03	17.8	7.3

The range of source depths calculated here could be related to (i) shallow intrusion(s) that likely act as a heat source to MGS and/or (ii) a mid-crustal magma reservoir beneath the volcanic complex (as obtained by Reyes-Wagner et al. (2017) through 2D magnetotelluric inversion). Within this range of depths, small magnitude (< 3 M_L) volcano

674 tectonic events near the volcanic edifice have been reported (OVDAS, *Observatorio*
675 *Volcanológico de los Andes del Sur*). The values of source depths calculated, represent
676 the long-term location of the plumbing system of the volcanic complex, and should be
677 complemented with other geophysical (seismic tomography, active seismicity, gravity)
678 and geochemical methods (mineral chemistry, geobarometry) to reduce uncertainty.

679 Several studies have already attempted to estimate the overpressure and source depths
680 of magmas using the aforementioned technique in other volcano tectonic settings (e.g.
681 Ray et al., 2006; Becerril et al., 2013; Browning et al., 2015; Elshaafi and Gudmundsson,
682 2016; Karaoglu et al., 2018; Drymoni et al., 2020). Nonetheless, analytical calculation of
683 magma overpressure and magma source depth is also highly sensitive to dyke aspect
684 ratios and the appropriate choice of crustal stiffness (Young's modulus). Further studies
685 are needed to confirm general relations between magmatic driving pressures and aspect
686 ratios of dykes and other fluid filled fractures in Andean settings.

687

688 **5.3. Dynamic paleo stress reconstruction and the role of dyke injections in local**
689 **stress field rotations**

690 The paleo stress reconstruction from dyke orientation data indicates an extensional stress
691 regime at the time of dyke formation, with a horizontal NNW-trending minimum
692 compressive stress (σ_3 and steeply dipping maximum compressive stress σ_1 (Figure 8a).
693 This paleostress state partly explains the overall ENE orientation of the dyke swarm and
694 we suggest that this result describes a "bulk" tectonic stress field, since it does not
695 necessarily explain all the dyke orientations observed in the dyke swarm. Dyke strike
696 ranges almost 90º, with a high concentration of dykes striking between N30ºE and N90ºE
697 (n=27), with two preferential orientations observed that appear to cross-cut each other:
698 (1) N50º-70ºE (n=10) and (2) N70º-90ºE (n=12) (Figure 6, 7c), which we expected to
699 represent two stress states. The stress inversion method used here is highly sensitive to
700 outlier orientations (e.g. dyke 1.1), and therefore the resulting stress field could be subject
701 to debate. The stress ratio obtained from the inversion and the 95% confidence ellipse of
702 the least and intermediate principal stress axes (Figure 8a) (as seen in the stereoplot)

703 indicate that the least and intermediate principal stresses could have rotated and
704 swapped.

705 Dykes are dynamic features that influence their surrounding stress field by locally
706 compressing the crust in orientations perpendicular to their strike to facilitate opening (e.g.
707 Roman & Cashman, 2006; Tibaldi & Bonali, 2017). Hence, the emplacement of any one
708 dyke influences the stress field and the orientation of later dyke emplacement events. In
709 Figures 10 and 11 (a, c) of our numerical results, we note that tensile stress is generated
710 at the tips of the pressurized dykes of a sufficient magnitude to promote hydrofracture,
711 dilation and the continuation of the dyke propagation path. At the tips of the dykes, the
712 trajectories of σ_1, have a ~60º range ($\pm$30º) in the absence of a regional tectonic load, but
713 that range is reduced to nearly ~40º ($\pm$20º) when we add a horizontal compression. These
714 findings suggest that dykes do not necessarily emplace following a “bulk” stress field, but
715 instead form over a wider range of orientations that takes account of both the bulk stress
716 field and local stress anisotropy, as for example, that generated by a previous dyke
717 injection. Nonetheless, the effect of a far field stress regime remains the most important
718 control on regional dyke swarms, as we observe from our numerical models that σ_1 rotates
719 in the direction of the regional stress field and therefore dyke propagation paths seek to
720 maintain their orientation parallel to a plane of principal stress.

721 From our field observations and the numerical models, it is possible to consider the
722 evolution of the studied dyke swarm as follows:

723 Injection of a basaltic magma through ENE-striking sub-vertical dykes from either shallow
724 or mid-crustal magmatic reservoirs (~8-13 km depth) beneath the TSPP volcanic
725 complex. Injection of these dykes alters the stress field, rotating the σ_H trajectories to a
726 ~60º range of orientations between N50ºE and N110ºE. Preferential injection of NE-
727 striking vertical dykes again rotates the trajectories of σ_H and influences the propagation
728 path of later dykes. Injection of these dykes also, in turn, alters the stress field, and σ_H
729 trajectories rotate to a ~60º range between N25ºE and N95ºE (Figure 12). The effect of
730 regional tectonic compression is to reduce the range of angles over which any new dyke
731 segment can become emplaced (Figure 12b). This result is supported by observations
732 from laboratory true-triaxial deformation experiments which indicate that the range of

angles over which new mode I fractures grow is reduced when the level of applied horizontal stress is greater (Browning et al., 2017), in that case the horizontal stress is the intermediate principal stress.

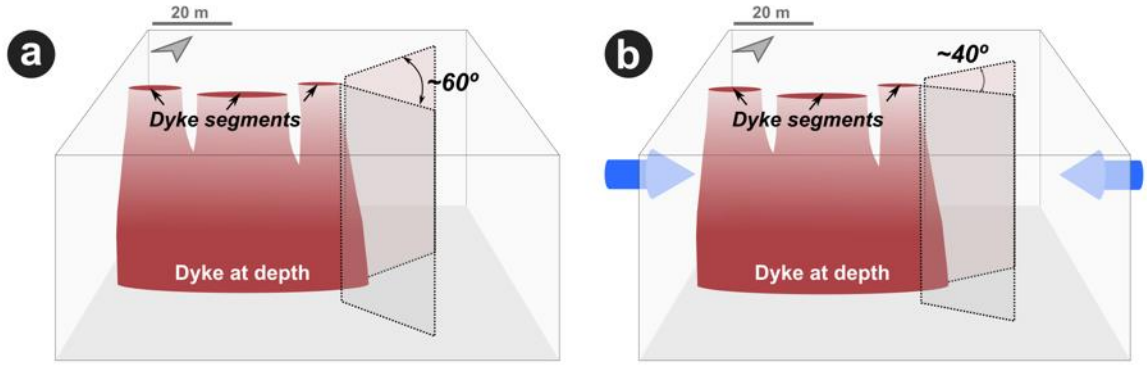

Figure 12: Cartoon showing (a) the influence of dyke injections on the range of possible propagation pathways of future dyke injections. (b) When considering a far field compression (the blue arrows), the range of potential orientations is reduced by 20º.

5.4. Emplacement model and regional geological implications

The ENE oriented Tatara-San Pedro-Pellado volcanic chain is characterized by abundant ENE-striking dykes and minor eruptive vents, such as the feeder dyke swarm described here. In the Southern Andes, this orientation of volcanism can also be observed at the NE oriented Callaqui stratovolcano and dyke swarms, which is formed in an overall dextral transpressional setting (Sielfeld et al., 2017) and at the Llaima-Sierra Nevada volcanic chain (Naranjo and Moreno, 2005). These examples suggest that Pleistocene-Holocene magma migration has occurred in ENE oriented pathways, driven by a combination of both Quaternary intra arc ENE trending shortening (Lavenu and Cembrano, 1999; Cembrano and Lara, 2009) and optimally oriented fault-fracture systems.

The paleo stress reconstruction from dyke orientation agrees with the fault-slip and dyke orientation paleo-stress inversion in the same area (Sielfeld et al., 2019b) and aids in the definition of the Tatara-Damage Zone, a ca. 4 km wide and 9 km long graben-like transtensional block over which the TSPP is constructed. transtensional block within the volcanic complex. This block, namely, the Tatara Damage Zone, is a ca. 8 km wide and

12 km long graben-like structure beneath the main volcanic edifice. It is characterized predominantly by NE-ENE oblique slip transtensional faults and dykes. Faulting activity within this structure is long-lived (late Miocene up to late Pleistocene) and could have helped develop the construction of the volcanic complex by providing active pathways for interseismic eruptive activity, as well as the heat source and permeability structures for the emplacement of a geothermal reservoir (MGS) (Hickson et al., 2011; Sielfeld et al., 2019b).

Resistivity models from magnetotelluric data inversion show a wide conductive region from the volcanic front at this latitude to the east (Reyes-Wagner et al., 2017). Three conductive bodies, related to three distinct magmatic-hydrothermal bodies, are associated with TSPP, MGS and LDM. Reyes-Wagner et al. (2017) correlated the deepest and largest anomaly (~8-10 km deep) to a magma reservoir melt at the volcanic front (TSPP), and associated the shallow body (~3 km deep) with the heat source for the high enthalpy MGS. The source depths obtained from the analytical method used in this study agree with Reyes-Wagner et al. (2017) models: shallow depths (< 5km) obtained from our calculations could be correlated to a magmatic heat source for MGS, while deep depths could be associated with deeper crustal reservoirs. The latter could also be supported with the dykes more primitive composition. The mafic rock composition of the dykes and volcanic products of the TSPP also indicate a more primitive composition most likely derived from a deeper source.

It is reasonably assumed that most dykes possess a strike dimension significantly smaller than their dip dimension, indicating vertical propagation. The geometry of the dyke swarm, made up of several offset segments, is also indication that the dykes likely propagated predominantly vertically (Gudmundsson, 1990; Ray et al., 2006), although we do not rule out the possibility of some lateral propagation. However, whether the dykes propagated vertically or laterally bears no impact on the described mechanical controls on the strike orientations. The exposed feeder dyke(s) of this swarm are the near-surface representation of likely only a mere 10-20% of the dykes that may have initially propagated from a deeper magmatic source (e.g. Menand et al., 2010). The remaining majority of 80-90% of the rest of the dykes would have be arrested or deflected into sills at depth (Gudmundsson, 2006). We propose that the dykes in the TSPP propagated

vertically from a deep magmatic reservoir and that the arrest and deflection of dykes into sills at ~2-3 km has served to mature the heat source and generation of the active (MGS) hydrothermal system (Figure 13).

Figure 13: Cartoon of the Tatara-San Pedro volcanic complex and the plumbing system in depth. The Mariposa Geothermal System anomaly (Hickson et al., 2011) is projected in the surface and represented with a segmented green line. Two depths of origin are proposed for the dyke swarm: (1) from a deep magmatic reservoir and (2) shallow magmatic reservoir (C1 and C2 conductive anomalies as presented by Reyes-Wagner et al. (2017) and by Hickson et al., (2011)).

6. CONCLUSIONS

1. We studied a near surface section of a feeder dyke system, ~5 km to the east of the Pellado volcano (Southern Volcanic Zone of Chile). This area lies directly above a conductive anomaly which has previously been interpreted as an active geothermal system (Mariposa Geothermal System; MGS). In total, 35 dyke segments were measured, some of which likely fed a fissure eruption, as indicated by *flow like* and vesicular textures in some dykes an intrusion into a minor eruptive centre.
2. Analytical estimates of the depth of magma origin from aspect ratios of 33 dyke segments indicate a range of depths between 2.7 and 22.8 km and mean depth of 8-km for the origin of the magma (8 – 13 km). This range of depths represents the long-term location of the plumbing system of the volcanic complex, and could be related to shallow crustal reservoirs or to deeper reservoirs associated with a ~8-10 km deep conductive anomaly previously observed with 2D magnetotelluric inversion (Reyes-Wagner et al., 2017) in the volcanic arc region, and from petrographical analysis of the dykes. From these observations, we hypothesize that magma propagated vertically from a magmatic reservoir from a roof at around 8-10 km depth. Magma was transported directly to the surface from this chamber, to feed eruptions, as was the case with the dyke swarm studied. However, it is possible that magma from the deep reservoir has been transported to shallower crustal levels where it is arrested and acts as a heat source for the generation of the previously identified MGS.
3. Our two-dimensional finite element models show that a combination of both internal magma pressure and regional tectonic compressive loading locally rotate crustal principal stresses. Rotation is exacerbated when the crust hosts heterogeneities, such

as previous dyke injections. The effect is to locally rotate the principal stress orientations and locally increase the magnitude of the bedrock's tensile stress. These effects combine to influence the trajectories over which new dyke injections will propagate and hence the arrangement of shallow magmatic plumbing systems, as well as the distribution of heat sources for hydrothermal systems.

4. We find that individual dyke injections themselves can locally rotate the orientation of the principal stresses if the regional tectonic loading direction is somewhat offset from the dyke strike. The effect again, is that previous dyke injection events modify the propagation paths of future dyke injections. This finding should be considered during periods of unrest, and for volcanic hazard assessments, when considering the location and orientation of secondary fissure eruptions in active volcanic areas such as the Southern Volcanic Zone of Chile.

ACKNOWLEDGEMENTS

This research is supported by FONDAP project 15090013 CEGA (Centro de Excelencia en Geotermia de los Andes), FONDECYT project 1141139 to J.C. and FONDECYT project 11190143 to J.B. Chilean-French scientific cooperation via the ECOS Project 180027/PC18U08 is also acknowledged. We thank the editor, Dr. Diana Roman, and Journal referees Dr. Alessandro Tibaldi and an anonymous reviewer for providing thorough reviews that helped to improve the text. Dr. Gloria Arancibia and Dr. Luis Lara are thanked for their comments to an earlier version of this manuscript, which is part of the first author's Master of Science thesis at Pontificia Universidad Católica de Chile. We thank Leonardo Carrasco from Energy Development Company (previously Magma Energy Chile) for helping us get access to their concessions to carry out field work.

REFERENCES

Acocella, V. & Neri, M., 2009. Dike propagation in volcanic edifices: overview and possible developments. Tectonophysics, 471(1-2), pp.67-77.

Acocella, V & Funiciello, F., 2010. Kinematic setting and structural control of arc volcanism. Earth and Planetary Science Letters. 289, 43-53. http://dx.doi.org/10.1016/j.epsl.2009.10.027.

Ágústsdóttir, T., Woods, J., Greenfield, T., Green, R.G., White, R.S., Winder, T., Brandsdóttir, B., Steinthórsson, S., Soosalu, H., 2016. Strike-slip faulting during the 2014 Bárðarbunga-Holuhraun dike intrusion, central Iceland. Geophysical Research Letters, 43(4), 1495-1503. https://doi.org/10.1002/2015GL067423

Ágústsdóttir, T., Winder, T., Woods, J., White, R. S., Greenfield, T., & Brandsdóttir, B., 2019. Intense seismicity during the 2014-2015 Bárðarbunga-Holuhraun rifting event, Iceland, reveals the nature of dike-induced earthquakes and caldera collapse mechanisms. Journal of Geophysical Research: Solid Earth, 124, 8331– 8357. https://doi.org/10.1029/2018JB016010

Anderson, E. M., 1951. The dynamics of faulting and dyke formation with applications to Britain [Book]. Hafner Pub. Co.

Andrew, R.E.B & Gudmundsson, A., 2008. Volcanoes as elastic inclusions: their effects on the propagation of dykes, volcanic fissures, and volcanic zones in Iceland. J Volcanol Geotherm Res 177:1045– 1054. doi:10.1016/j.jvolgeores.2008.07.025

Angermann, D., Klotz, J., Reigber, C., 1999. Space-geodetic estimation of the Nazca-south America Euler vector. Earth Planetary Science Letters. 171, 329–334. https://doi.org/10.1016/S0012-821X(99)00173-9.

Aravena, D., Muñoz, M., Morata, D., Lahsen, A., Parada, M. A., & Dobson, P., 2016. Assessment of high enthalpy geothermal resources and promising areas of Chile. Geothermics, 59 , 1-13. Retrieved from http://www.sciencedirect j.geothermics.2015.09.001

Baer. G & Beyth. M., 1990. A mechanism of dyke segmentation in fractured host rock. In: Parker AJ, Rickwood PC, Tucker DH (eds) Mafic dykes and emplacement mechanisms. Balkema, Rotterdam, pp 3–11

Becerril L, Galindo I, Gudmundsson A, Morales J.M., 2013 Depth of origin of magma in eruptions. Sci Rep 3:2763. doi:10.1038/srep02762.

Browning, J., Drymoni, K., Gudmundsson, A., 2015. Forecasting magma-chamber rupture at Santorini volcano, Greece. Scientific Reports, 5, 15785, 10.1038/srep15785.

Browning, J., Meredith, P.G., Stuart, C.E., Healy, D., Harland, S. and Mitchell, T.M., 2017. Acoustic characterization of crack damage evolution in sandstone deformed under conventional and true triaxial loading. Journal of Geophysical Research: Solid Earth, 122(6), pp.4395-4412.

Cardona, C., Tassara, A., Gil-Cruz, F., Lara, L., Morales, S., Kohler, P., & Franco, L., 2018. Crustal seismicity associated to rapid surface uplift at Laguna del Maule Volcanic Complex, Southern Volcanic Zone of the Andes. Journal of Volcanology and Geothermal Research, 353(January), 83–94. https://doi.org/10.1016/j.jvolgeores.2018.01.009

Cembrano, J., & Lara, L., 2009. The link between volcanism and tectonics in the southern volcanic zone of the Chilean Andes: A review. Tectonophysics, 471(1–2), 96–113. https://doi.org/10.1016/j.tecto.2009.02.038

Cerpa, N. G., Araya, R., Gerbault, M., & Hassani, R., 2015. Relationship between slab dip and topography segmentation in an oblique subduction zone: Insights from numerical modeling. Geophysical Research Letters, 42, 5786–5795. https://doi.org/10.1002/2015GL064047

Charrier, R., Baezar, O., Elgueta, S., Flynn, J.J., Gans, P., Kay, S.M., Muñoz, N., Wyss, A.R., Zurita, E., 2002. Evidence for Cenozoic extensional basin development and tectonic inversion south of the flat-slab segment, southern Central Andes, Chile (33°-36°S). Journal of South American Earth Sciences 15, 117–1139.

Chery, J., Zoback, M. D., & Hassani, R., 2001. An integrated mechanical model of the San Andreas fault in central and northern California. Journal of Geophysical Research, 106(B10), 22051–22066.

Chouet, B.A., 1996. Long-period volcano seismicity: its source and use in eruption forecasting. Nature380 (6572), 309–316.

Cordell, D., Unsworth, M. J., & Díaz, D., 2018. Imaging the Laguna del maule volcanic field, central chile using magnetotellurics: Evidence for crustal melt regions laterally offset from surface vents and lava flows. Earth and Planetary Science Letters, 488, 168-180. doi: https://doi.org/10.1016/j.epsl.2018.01.007

Contreras, M., Tassara, A., Gerbault, M., Araya, R., Bataille, K., 2016. Deformacion interssmica en zonas de subduccion investigada por modelos numricos 2D: Estudio de caso antes del terremoto del Maule 2010. Andean Geology, 43(3), 247–262.

Costa, F., Singer, B., 2002 Evolution of Holocene dacite and compositionally zoned magma, Volcán San Pedro, Southern Volcanic Zone, Chile. Journal of Petrology, 43, 1571-1593. https://doi.org/10.1093/petrology/43.8.1571.

Cundall, P.A., Board, M., 1988. A microcomputer program for modeling large-strain plasticity problems. Numerical Methods in Geomechanics, 6, 2101-2108.

Dahm, T., 2000a. Numerical simulations of the propagation path and the arrest of fluid-filled fractures in the Earth. Geophysical Journal International, 141, 623-638.

Daniels, K.A., Kavanagh, J.L., Menand, T. & Stephen, J.S.R., 2012. The shapes of dikes: evidence for the influence of cooling and inelastic deformation, Bull. geol. Soc. Am., 124(7–8), 1102–1112.

Davidson, J. P., Ferguson, K. M., Colucci, M. T., Dungan, M. A., 1988. The origin and evolution of magmas from the San Pedro-Pellado volcanic complex, S. Chile: multicomponent sources and open system evolution. Contributions to Mineralogy and Petrology, 100(4), 429–445. https://doi.org/10.1007/BF00371373

Delaney, P. T., Pollard, D. D., 1981. Deformation of host rocks and flow of magma during growth of minette dikes and breccia-bearing intrusions

Delaney, P. T., Pollard, D. D., Ziony, I., & McKee, E. H. ., 1986. Field relations between dikes and joints: emplacement processes and paleostress analysis. Journal of Geophysical Research, 91(5), 4920–4938.

928 Drymoni, K., Browning, J., Gudmundsson, A., 2020. Dyke-arrest scenarios in extensional
929 regimes: Insights from field observations and numerical models, Santorini, Greece.
930 Journal of Volcanology and Geothermal Research, 396, 106854,
931 https://doi.org/10.1016/j.jvolgeores.2020.106854

932 Dungan, M., Wulff, A., Thompson, R., 2001. Eruptive stratigraphy of the Tatara-san Pedro
933 Complex, 36°S, Southern Volcanic Zone, Chilean Andes: reconstruction method and
934 implications for magma evolution at long-lived arc volcanic centers. J. Petrol. 42 (3p),
935 555–626. https://doi.org/10.1093/petrology/42.3.555.

936 Elshaafi, A., Gudmundsson, A., 2016. Volcano-tectonics of the Al Haruj Volcanic
937 Province, Central Libya. Journal of Volcanology and Geothermal Research, 325, 189-
938 202. https://doi.org/10.1016/j.jvolgeores.2016.06.025

939 Emerman, S. H., & Marrett, R., 1990. Why dikes? Geology, 18, 231-233.
940 https://doi.org/10.1130/0091-7613(1990)018<0231

941 Espinosa, J., 2019. Significado tectónico del emplazamiento de diques y centros
942 eruptivos menores en el sector de Cerro Negro (36ºS), Zona Volcánica Sur Transicional
943 de los Andes. (Undergraduate Thesis). Universidad de Concepción, Concepción, Chile.

944 Faye, G. D., Yamaji, A., Yonezu, K., Tindell, T., & Watanabe, K., 2018. Paleostress and
945 fluid-pressure regimes inferred from the orientations of Hishikari low sulfidation epithermal
946 gold veins in southern Japan. Journal of Structural Geology, 110(October 2017), 131–
947 141. https://doi.org/10.1016/j.jsg.2018.03.002

948 Galland, O., de Bremond d'Ars, J., Cobbold, P.R., Hallot, E., 2003. Physical models of
949 magmatic intrusion during thrusting. Terra Nova 15, 405–409.

950 Galland, O., Hallot, E., Cobbold, P.R., Ruffet, G., de Bremond d'Ars, J., 2007. Volcanism
951 in a compressional Andean setting: a structural and geochronological study of Tromen
952 volcano (Neuquén province, Argentina). Tectonics 26. doi:10.1029/2006TC002011.

953 Gerbault, M., Cappa, F., Hassani, R., 2012. Elasto-plastic and hydromechanical models
954 of failure around an infinitely long magma chamber. Geological Society, London, Special
955 Publications, 367, 111-130. https://doi.org/10.1144/SP367.8

Gerbault, M., Hassani, R., Lizama, C. N., & Souche, A., 2018. Three-dimensional failure patterns around an inflating magmatic chamber. Geochemistry, Geophysics, Geosystems, 19, 749–771. https://doi.org/10.1002/2017GC007174

Geshi, N., Kusumoto, S., Gudmundsson, A., 2010. The geometric difference between non-feeders and feeder dykes. Geology, 38, 195-198.

Geshi, N., Browning, J. and Kusumoto, S., 2020. Magmatic overpressures, volatile exsolution and potential explosivity of fissure eruptions inferred via dike aspect ratios. Scientific Reports, 10(1), pp.1-9.

Giambiagi, L., Ramos, V.A., 2002. Structural evolution of the Andes in a transitional zone between flat and normal subduction (33º30'–33º45'S), Argentina and Chile. Journal of South American Earth Sciences, 15, 99–114.

González, O., and Vergara, M., 1962. Reconocimiento geológico de la Cordillera de los Andes entre los paralelos 35 y 38 sur.

Griffith, A.A., 1921. The phenomena of rupture and flow in solids. Phil. Trans. R. Soc. A221, 163.

Gudmundsson, A., Andrew, R.E.B., 2007. Mechanical interaction between active volcanoes in Iceland. Geophysical Research Letters 34, L10310. doi:10.1029/2007GL029873.

Gudmundsson, A., 1990. Emplacement of dikes, sills and crustal magma chambers at divergent plate boundaries. Tectonophysics 176 (3), 257–275.

Gudmundsson, A., 2002. Emplacement and arrest of sheets and dykes in central volcanoes. Journal of Volcanology and Geothermal Research, 116, 279–298.

Gudmundsson, A., 2006. How local stresses control magma-chamber ruptures, dyke injections, and eruptions in composite volcanoes. Earth Sci. Reviews, 79(1–2), 1–31.

Gudmundsson A., 2011 Rock fractures in geological processes. Cambridge University Press, Cambridge

Gudmundsson, A., Lecoeur, N., Mohajeri, N., Thordarson, T., 2014. Dike emplacement at Bardarbunga, Iceland, induces unusual stress changes, caldera deformation, and earthquakes. Bulletin of Volcanology, 76 (869), 1-7. DOI 10.1007/s00445-014-0869-8

Gudmundsson, A., 2020. Volcanotectonics: Understanding the Structure, Deformation and Dynamics of Volcanoes. Cambridge University Press.

Gudmundsson, M.T., Jónsdóttir, K., Hooper, A., Holohan, E.P., Halldórsson, S.A., Ófeigsson, B.G., Cesca, S., Vogförd, K.S., Sigmundsson, F., Högnadóttir, T., Einarsson, P., Sigmarsson, O., Jarosh, A.H., Jónasson, K., Magnússon, E., Hreinsdóttir, S., Bagnardi, M., Parks, M.M., Hjörleifsdóttir, V., Pálsson, F., Walter, T.R., Schöpfer, M.P.J., Heimann, S., Reynolds, H.I., Dumont, S., Bali, E., Gudfinnsson, G.H., Dahm, T., Roberts, M.J., Hensch, M., Belart, J.M.C., Spaans, K., Jakobsson, S., Gudmundsson, G.B., Fridriksdóttir, H.M., Drouin, V., Dürig, T., Aðalgeirsdóttir, G., Riishuus, M., Pedersen, G.B.M., van Boeckel, T., Oddsson, B., Pfeffer, M., Barsotti, S., Bergsson, B., Donovan, A., Burton, M.R & Aiuppa, A., 2016. Gradual caldera collapse at Bárðarbunga volcano, Iceland, regulated by lateral magma outflow. Science, 353, 6926. 10.1126/science.aaf8988

Hassani, R., Jongmans, D., & Chery, J., 1997. Study of plate deformation and stress in subduction processes using two-dimensional numerical models. Journal of Geophysical Research, 102(B8), 17951–17965.

Heap, M. J., Villeneuve, M., Albino, F., Farquharson, J. I., Brothelande, E., Amelung, F., Got., J. & Baud, P., 2020. Towards more realistic values of elastic moduli for volcano modelling. Journal of Volcanology and Geothermal Research, 390, 106684.

Hickson, C.J., Ferraris, F., Rodriquez, C., Sielfeld, G., Henriquez, R., Gislason, T., Selters, J., Benoit, D., White, P., Southon, J., Ussher, G., Charroy, J., Smith, A., Lovelock, B., Lawless, J., Quinlivan, P., Smith, L & Yehia, R., 2011. The Mariposa geothermal system, Chile, in: Transactions - Geothermal Resources Council. pp. 817–825.

Hildreth, W & Moorbath, S., 1988. Crustal contributions to arc magmatism in the Andes of Central Chile. Contrib. Mineral. Petrol. 98, 455–489. https://doi.org/10.1007/BF00372365.

1011 Hildreth, W., Godoy, E., Fierstein, J., Singer, B., 2010. Laguna del Maule Field. Eruptive
1012 history of a quaternary basalt-to-rhyolite distributed volcanic field on the Andean range
1013 crest in central Chile. Boletin No 63, 2010. Subdirección Nacional de
1014 Geología.Sernageomin.

1015 Hill, D.P., 1977. A model for earthquake swarms. Journal of Geophysical Research, 82(8),
1016 1347–1352. https://doi.org/10.1029/jb082i008p01347

1017 Hoek, J.D., 1991. A classification of dyke-fracture geometry with examples from
1018 Precambrian dyke swarms in the Vestfold Hills, Antarctica. Geol Rundsch 80, 233–248.
1019 https://doi.org/10.1007/BF01829363

1020 Jolly, R.J.H., Sanderson, D.J., 1997. A Mohr circle construction for the opening of a pre-
1021 existing fracture. J. Struct. Geol. 19, 887–892. https://doi.org/10.1016/S0191-
1022 8141(97)00014-X

1023 Kalakay, Thomas J., John, B.E., Lageson, D.R., 2001. Fault-controlled pluton
1024 emplacement in the Sevier fold-and-thrust belt, SW Montana. Journal of Structural
1025 Geology 23, 1151–1165.

1026 Karaoglu, Ö., Browning, J., Salah, M.K., Elshaafi, A., Gudmundsson, A., 2018. Depths of
1027 magma chambers at three volcanic provinces in the Karliova region of Eastern Turkey.
1028 Bulletin of Volcanology.

1029 Kavanagh, J., Menand, T., Sparks, R.S.J., 2006. An experimental investigation of sill
1030 formation and propagation in layered elastic media. Earth and Planetary Science Letters.
1031 245, 799-813.

1032 Lavenu, A., Cembrano, J., 1999. Compressional and transpressional stress pattern for
1033 the Pliocene and Quaternary (Andes of central and southern Chile). J. Struct. Geol. 21,
1034 1669–1691. https://doi.org/10.1016/S0191-8141(99)00111-X.

1035 Li, D., Zhu, Q., Zhou, Z., Li, X., Ranjith, P.G., 2017. Fracture analysis of marble specimens
1036 with a hole under uniaxial compression by digital image correlation. Engineering Fracture
1037 Mechanics, 183, 109-124.

López-Escobar, L., Cembrano, J., Moreno, H., 1995. Geochemistry and tectonics of the Chilean Southern Andes basaltic Quaternary volcanism. Andean Geol. 22, 219–234. https://doi.org/10.5027/andgeoV22n2-a06.

Maccaferri, F., Bonafede, M., Rivalta, E., 2011. A quantitative study of the mechanisms governing dike propagation, dike arrest and sill formation. Journal of Volcanology and Geothermal Research. 208, 39-50.

Menand, T., Daniels, K.A., Benghiat, P., 2010. Dyke propagation and sill formation in a compressive tectonic environment. Journal of Geophysical Research, 115, B08201, doi:10.1029/2009JB006791.

Muñoz, B.J., Niemeyer, R.H., 1984. Hoja Laguna del Maule: regiones del Maule y del Biobio, Carta Geológica de Chile 1:250000. Servicio Nacional de Geología y Minería, Santiago, Chile.

Nakamura, K., 1977. Volcanoes as possible indicators of tectonic stress orientation - principle and proposal. Journal of Volcanology and Geothermal Research, 2(1), 1–16. https://doi.org/10.1016/0377-0273(77)90012-9

Naranjo, J.A., Moreno, H., 2005. Geología del volcan Llaima, Region de la Araucanía. Servicio Nacional de Geología y Minería, Carta Geologica de Chile. In: Serie Geología Basica, vol. 88, p. 33. Mapa escala 1:50.000, Santiago.

Novoa, C., Rémy, D., Gerbault, M., Baes, J.C., Tassara, A., Cordova, L., Cardona, C., Granger, M., Bonvalot, S., Delgado, F., 2019. Viscoelastic relaxation: a mechanism to explain the decennial large surface displacements at the Laguna del Maule silicic volcanic complex. Earth Planet. Sci. Lett. 521, 46–59. https://doi.org/10.1016/j.epsl.2019.06.005.

Pardo-Casas, F & Molnar, P., 1987. Relative motion of the Nazca (Farallon) and South American plates since late cretaceous time. Tectonics 6, 233–248.

Pearce, R. K., Sánchez de la Muela, A., Moorkamp, M., Hammond, J.O.S., Mitchell, T.M., Cembrano, J., Araya Vargas, J., Meredith, P.G., Iturrieta, P., Pérez-Estay, N., Marshall, N.R., Smith, J., Yañez, G., Griffith, W.A., Marquardt-Román, C., Stanton-Yonge, A & Núñez, R., 2020. Interaction between hydrothermal fluids and fault systems in the in the

Southern Andes revealed by magnetotelluric and seismic data. Earth and Space Science Open Archive, (November), 1–32. https://doi.org/10.1002/essoar.10501143.1

Pérez-Flores, P., Cembrano, J., Sanchez, P., Veloso, E., Arancibia, G., Roquer, T., 2016. Tectonics, magmatism and paleo-fluid distribution in a strike-slip setting: Insights from the northern termination of the Liquiñe-Ofqui fault System, Chile. Tectonophysics 680, 192–210. https://doi.org/10.1016/j.tecto.2016.05.016

Piquer, J., Yañez, G., Rivera, O., & Cooke, D. R., 2018. Long-lived crustal damage zones associated with fault intersections in the high Andes of central chile [Journal Article]. Andean Geology, 46 (2), 223-239.

Ray, R., Sheth, H., Mallik, J., 2006. Structure and emplacement of the Nandurbar–Dhule mafic dyke swarm, Deccan Traps, and the tectonomagmatic evolution of flood basalts. Bulletin of Volcanology, 69, 537-551. DOI 10.1007/s00445-006-0089-y

Reyes-Wagner, V., Díaz, D., Cordell, D., Unsworth, M., 2017. Regional electrical structure of the Andean subduction zone in central Chile (35°–36°S) using magnetotellurics. Earth Planets Space 69, 142–151. https://doi.org/10.1186/s40623-017-0726-z.

Roman, D. C., & Cashman, K. V., 2006. The origin of volcano-tectonic earthquake swarms. Geology, 34(6), 457–460. https://doi.org/10.1130/G22269.1

Rooney, T. O., I. D. Bastow, and D. Keir., 2011, Insights into extensional processes during magma assisted rifting: evidence from aligned scoria cones, J. Volcanol. Geotherm. Res., 201(1–4), 83–96.

Rubin, A. M., 1995. Propagation of Magma-Filled Cracks. Annual Review of Earth and Planetary Sciences, 23(1), 287–336. https://doi.org/10.1146/annurev.ea.23.050195.001443

Shaw, H. R., 1980. The fracture mechanisms of magma transport from the mantle to the surface. In Physics of magmatic processes, 64 , 201-264.

Sielfeld, G., Cembrano, J., & Lara, L., 2017. Transtension driving volcano-edifice anatomy: Insights from Andean transverse-to-the-orogen tectonic domains [Journal Article]. Quaternary International .

1094 Sielfeld, G., Ruz, J., Brogi, A., Cembrano, J., Stanton-Yonge, A., Pérez-Flores, P.,
1095 Iturrieta, P., 2019. Oblique-slip tectonics in an active volcanic chain: A case study from
1096 the Southern Andes. Tectonophysics, 770. https://doi.org/10.1016/j.tecto.2019.228221

1097 Sigmundsson, F., Hooper, A., Hreinsdóttir, S., Vogfjörd, K.S., Ófeigsson, B.G.,
1098 Heimisson, E.R., Dumont, S., Parks, M., Spaans, K., Gudmundsson, G.B., Drouin, V.,
1099 Árnadóttir, T., Jónsdóttir, K., Gudmundsson, M.T., Högnadóttir, T., Fridriksdóttir, H.M.,
1100 Hensch, M., Einarsson, P., Magnússon, E., Samsonov, S., Brandsdóttir, B., White, R.S.,
1101 Ágústsdóttir, T., Greenfield, T., Green, R.G., Hjartardóttir, A.R., Pedersen, R., Bennett,
1102 R.A., Geirsson, H., La Femina, P.C., Björnsson, H., Pálsson, F., Sturkell, E., Bean, C.J.,
1103 Möllhoff, M., Braiden, A.K & Eibl, E.P.S. 2015. Segmented lateral dyke growth in a rifting
1104 event at Bárðarbunga volcanic system, Iceland., 2015. Nature, 517 (7533), 191–195.

1105 Singer, B. S., Thompson, R. A., Dungan, M. A., Feeley, T. C., Nelson, S. T., Pickens, J.
1106 C., Brown, L.L., Wulff, A.W., Davidson, J.P & Metzger, J., 1997. Volcanism and erosion
1107 during the past 930 ky. at the Tatara-San Pedro complex, Chilean Andes. Bulletin of the
1108 Geological Society of America, 109(2), 127–142. https://doi.org/10.1130/0016-
1109 7606(1997)109<0127:VAEDTP>2.3.CO;2

1110 Spacapan, J., Galland, O., Leanza, H.A., Planke, S., 2016. Control of strike-slip fault on
1111 dyke emplacement and morphology. Journal of the Geological Society.
1112 doi:10.1144/jgs2015-166

1113 Stern, C. R., 2004. Active Andean volcanism: Its geologic and tectonic setting. Revista
1114 Geológica de Chile, 31(2), 161–206. https://doi.org/10.4067/S0716-02082004000200001

1115 Tapia, F., Farías, M., Naipauer, M., Puratich, J. (2015) Late Cenozoic contractional
1116 evolution of the current arc-volcanic region along the southern Central Andes (35º20'S).
1117 Journal of Geodynamics, 88, 36-51. http://dx.doi.org/10.1016/j.jog.2015.01.001

1118 Tassara, A., Yañez, G., 2003. Relación entre el espesor elástico de la litósfera y la
1119 segmentación tectónica del margen andino (15–47ºS). Rev. Geol. de Chile 30, 159–186.
1120 https://doi.org/10.4067/S0716-02082003000200002.

1121 Tibaldi, A., 2008. Contractional tectonics and magma paths in volcanoes. Journal of
1122 Volcanology and Geothermal Research, 176(2), 291-301.

Tibaldi, A., Vezzoli, L., Pasquaré, F. A., & Rust, D., 2008. Strike-slip fault tectonics and the emplacement of sheet–laccolith systems: the Thverfell case study (SW Iceland). Journal of Structural Geology, 30(3), 274-290.

Tibaldi, A., & Bonali, F. L., 2017. Intra-arc and back-arc volcano-tectonics: Magma pathways at Holocene Alaska-Aleutian volcanoes. Earth-Science Reviews, 167, 1-26.

Timoshenko, S., & Goodier, J. N., 1970. Theory of Elasticity (2nd ed., 608 pp.). New York: McGraw–Hill.

Woods, J., Donaldson, C., White, R.S., Caudron, C., Brandsdóttir, B., Hudson, T.S., Ágústsdóttir, T., 2018. Long-period seismicity reveals magma pathways above a laterally propagating dyke during the 2014-15 Bárðarbunga rifting event, Iceland. Earth and Planetary Science Letters, 490, 216-229. https://doi.org/10.1016/j.epsl.2018.03.020

Yamaji, A., & Sato, K., 2011. Clustering of fracture orientations using a mixed Bingham distribution and its application to paleostress analysis from dike or vein orientations. Journal of Structural Geology, 33(7), 1148–1157. https://doi.org/10.1016/j.jsg.2011.05.006

Yamaji, A., 2016. Genetic algorithm for fitting a mixed Bingham distribution to 3D orientations: A tool for the statistical and paleostress analyses of fracture orientations. Isl. Arc 25, 72–83. https://doi.org/10.1111/iar.12135